Pergamon

Geochimica et Cosmochimica Acta, Vol. 66, No. 10, pp. 1739–1757, 2002

0016-7037/02 $22.00 + .00

PII S0016-7037(01)00878-X

Effect of fluid–sediment reaction on hydrothermal fluxes of major elements, eastern flank of the Juan de Fuca Ridge

EMILY R. GIAMBALVO,[1,*,†] CARL I. STEEFEL,[2] ANDREW T. FISHER,[1,3] NINA D. ROSENBERG,[2] and C. GEOFFREY WHEAT[4]

[1]Earth Sciences Department, University of California, Santa Cruz, CA 95064, USA
[2]Energy and Environmental Sciences Directorate, Lawrence Livermore National Laboratory, Livermore, CA 94551, USA
[3]Institute of Tectonics, University of California, Santa Cruz, CA 95064, USA
[4]Global Undersea Research Unit, University of Alaska, Fairbanks, AK 99775, USA

(*Received April* 10, 2001; *accepted in revised form November* 19, 2001)

Abstract—On the eastern flank of the Juan de Fuca Ridge, reaction between upwelling basement fluid and sediment alters hydrothermal fluxes of Ca, $SiO_{2(aq)}$, SO_4, PO_4, NH_4, and alkalinity. We used the Global Implicit Multicomponent Reactive Transport (GIMRT) code to model the processes occurring in the sediment column (diagenesis, sediment burial, fluid advection, and multicomponent diffusion) and to estimate net seafloor fluxes of solutes. Within the sediment section, the reactions controlling the concentrations of the solutes listed above are organic matter degradation via SO_4 reduction, dissolution of amorphous silica, reductive dissolution of amorphous Fe(III)-(hydr)oxide, and precipitation of calcite, carbonate fluorapatite, and amorphous Fe(II)-sulfide. Rates of specific discharge estimated from pore-water Mg profiles are 2 to 3 mm/yr. At this site the basement hydrothermal system is a source of NH_4, $SiO_{2(aq)}$, and Ca, and a sink of SO_4, PO_4, and alkalinity. Reaction within the sediment column increases the hydrothermal sources of NH_4 and $SiO_{2(aq)}$, increases the hydrothermal sinks of SO_4 and PO_4, and decreases the hydrothermal source of Ca. Reaction within the sediment column has a spatially variable effect on the hydrothermal flux of alkalinity.

Because the model we used was capable of simulating the observed pore-water chemistry by using mechanistic descriptions of the biogeochemical processes occurring in the sediment column, it could be used to examine the physical controls on hydrothermal fluxes of solutes in this setting. Two series of simulations in which we varied fluid flow rate (1 to 100 mm/yr) and sediment thickness (10 to 100 m) predict that given the reactions modeled in this study, the sediment section will contribute most significantly to fluxes of SO_4 and NH_4 at slow flow rates and intermediate sediment thickness and to fluxes of $SiO_{2(aq)}$ at slow flow rates and large sediment thickness. Reaction within the sediment section could approximately double the hydrothermal sink of PO_4 over a range of flow rates and sediment thickness, and could slightly decrease (by $\leq$10%) the size of the hydrothermal source of Ca.

1. INTRODUCTION

The contribution of hydrothermal circulation through mid-ocean ridge crests and ridge flanks to the oceanic mass balance of some elements is comparable to the riverine contribution (Kadko et al., 1995). Although the composition of low-temperature hydrothermal fluids found on ridge flanks differs less from seawater than does that of high-temperature ridge-crest fluids, the larger volume of fluid that circulates through ridge flanks suggests that they may provide a similar or larger source or sink of several elements, including Mg, Ca, Si, and P (Mottl and Wheat, 1994; Kadko et al., 1995; Tréguer et al., 1995; Wheat et al., 1996). In ridge-flank environments a portion of the fluid entering and exiting the crust passes through the sediment section (e.g., Williams et al., 1979; Maris and Bender, 1982; Bender et al., 1985; Mottl, 1989; Wheat and McDuff, 1994, 1995; Wheat and Mottl, 1994; Davis et al., 1997; Fisher et al., 2001). Estimates of ridge-flank geochemical fluxes are derived from basement pore-water compositions (e.g., Wheat and Mottl, 2000) or from an accounting of basement alteration products (e.g., Alt and Teagle, 1999) and thus do not account for the influence of reactions within the sediment column on solute fluxes. In this article, we evaluate the effect of reaction between upwelling, basement-derived hydrothermal fluid and sediment on fluxes of Ca, SiO_2, SO_4, PO_4, NH_4, and alkalinity for two sites on the eastern flank of the Juan de Fuca Ridge.

Most studies of fluid advection through ridge flank sediments have used pore-water geochemical profiles to estimate flow rates and to identify reactions occurring in the sediment but have not attempted to quantify the influence of sediment diagenesis on hydrothermal fluid composition or vice versa. Exceptions include the diagenetic models of Wheat and McDuff (1994) and Wheat and Tribble (1994), which showed that upwelling hydrothermal fluids enhance amorphous silica dissolution and organic carbon degradation in the Mariana Mounds and result in the early transformation of amorphous silica to quartz in Middle Valley. In studies of sediment mineralogy, other effects of basement-derived hydrothermal fluid on sediment diagenesis have been documented, including early formation of chalks (Kastner et al., 1986) and replacement of calcareous–siliceous ooze with authigenic clays and oxides (Williams et al., 1979). These models and observations suggest that the reaction of upwelling, basement-derived hydrothermal fluid with sediment results in hydrothermal fluxes of solutes to and from the ocean that differ from the fluxes that result when basement fluid bypasses the sediment section.

* Author to whom correspondence should be addressed (ergiamb@sandia.gov).
† *Present address:* Sandia National Laboratories, Carlsbad, NM 88220, USA.

We used sediment pore-water geochemical data from Ocean Drilling Program (ODP) sites 1030 and 1031 (Davis et al., 1997; Mottl et al., 2000) to constrain a coupled reactive transport model of processes occurring in the sediment column. We included a full suite of major seawater species and a set of diagenetic reactions that are stoichiometrically consistent and whose rates of reaction are controlled by thermodynamic and kinetic constants. Because the model simulated the reaction mechanisms by which fluid composition changes, it could be used to evaluate the parameters controlling solute fluxes. We varied fluid flow rate and sediment thickness to determine the range of each over which upward seepage of hydrothermal fluid through sediment alters hydrothermal fluxes. With respect to this emphasis on understanding the mechanisms that control sediment pore-water geochemistry, our study is similar to models of early diagenesis that seek to understand the processes controlling diffusive fluxes and burial fluxes of, for instance, P (Van Cappellen and Berner, 1988), $SiO_{2(aq)}$ (Rabouille et al., 1997), or Fe and Mn (Van Cappellen and Wang, 1996; Wang and Van Cappellen, 1996).

2. JUAN DE FUCA RIDGE FLANK

The Juan de Fuca Ridge lies several hundred kilometers west of the North American continent (Fig. 1). A landward-thickening blanket of interbedded turbidites and hemipelagic clay deposited primarily during Pleistocene glaciation onlaps basalt 20 km east of the spreading center (Davis et al., 1997). Upward seepage of basement hydrothermal fluid through sediment occurs above a small basement high 40 km east of the spreading center (Wheat and Mottl, 1994; Davis et al., 1997). Upflow rates based on curvature in pore-water profiles of conservative elements range from 0.07 to 3.2 mm/yr (specific discharge) (Wheat and Mottl, 1994; Davis et al., 1997; this work).

Sediments at ODP sites 1030 and 1031 are hemipelagic clays and silts with interbedded silty turbidites. They contain calcite (2 to 40 wt% dry), phyllosilicates (30 to 50%), quartz (5 to 30%), feldspar (10 to 30%), pyrite (2 to 10%), and organic carbon (0.2 to 0.6%) (Davis et al., 1997). The sediment column maintains 60 to 80% porosity (average ~70%) throughout its thickness. Sedimentation rate has varied from 3 to 17 cm/ka and averages 4 to 6 cm/ka (Davis et al., 1997). Temperatures at the sediment–basement interface are 40.1°C and 40.4°C at ODP sites 1030 and 1031, respectively (Davis et al., 1997). Seepage rates are not fast enough to disturb linear thermal gradients.

The extensive pore-water geochemistry data set from ODP sites 1030 and 1031 includes concentrations of major seawater species, alkalinity, nutrients, and minor species such as Fe and F (Davis et al., 1997; Mottl et al., 2000) whose concentrations help constrain reactions affecting alkalinity and major species. At both sites pore-water samples were collected at 1.5- to 9.5-m intervals from 1.45 m below the seafloor (mbsf) to the base of the cored sediment section (5 m above the sediment–basement interface (41.7 mbsf) at ODP site 1030 and the sediment–basement interface (41.3 mbsf) at ODP site 1031) (Davis et al., 1997).

Pore fluids at the base of the sediment column are depleted in alkalinity, SO_4, and PO_4, and enriched in NH_4, Ca, and SiO_2 relative to bottom seawater (Davis et al., 1997). The pore fluid composition is similar to that of 64°C basement water collected 60 km to the east (Davis et al., 1997) and to that of hydrothermal fluid collected at warm springs on the Baby Bare basement outcrop, also located ~60 km to the east (Mottl et al., 1998; Wheat and Mottl, 2000). The similarities suggest that hydrothermal fluids at ODP sites 1030 and 1031 equilibrated with basement at a similarly high temperature (Davis et al., 1997; Elderfield et al., 1999) and that the site can be categorized as a "warm" (>45°C) hydrothermal site (Mottl and Wheat, 1994).

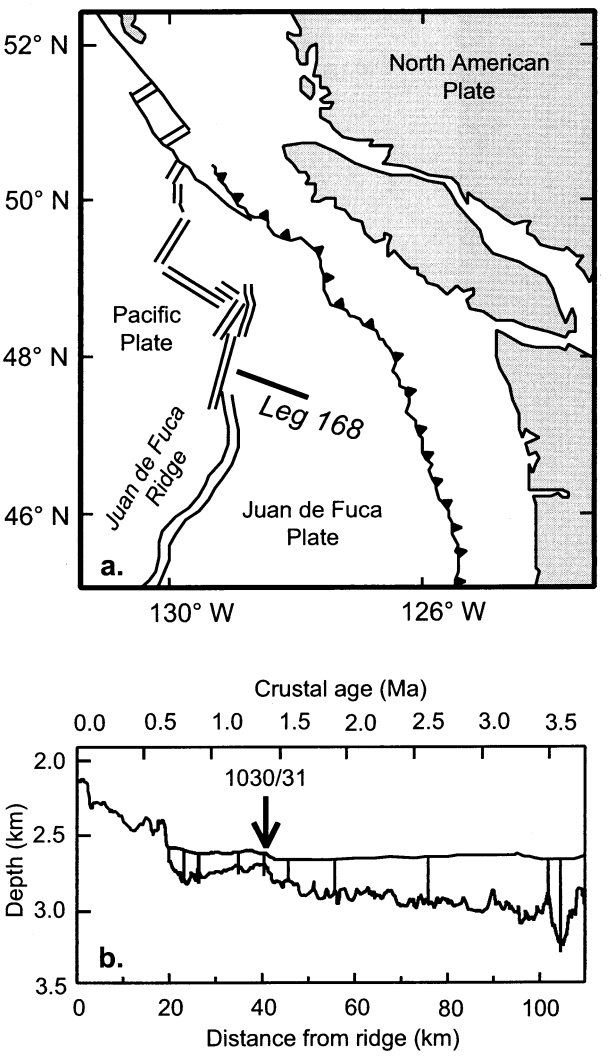

Fig. 1. (a) Juan de Fuca Ridge and location of the ODP leg 168 drilling transect (Davis et al., 1997). (b) Cross section of leg 168 transect and location of ODP sites 1030 and 1031 (Davis et al., 1997).

Warm sites have been discovered only on young (<6 Ma), rapidly sedimented crust, but reaction of seawater with basalt at warm sites could remove the entire river input of Mg if such sites account for only 8 to 20% of the total advective heat loss on ridge flanks (Mottl and Wheat, 1994). On the basis of the assumption that they remove 100% of river Mg, the composition of Baby Bare spring water suggests that warm sites could provide a source of Ca to the ocean as large as 39% of the river input and remove as much as 34% of the river input of SO_4 (Table 1) (Wheat and Mottl, 2000). Although ridge-flank hy-

Table 1. Estimated global fluxes from warm ridge-flank hydrothermal sites.

Species	Basement hydrothermal flux[a]		Sediment hydrothermal flux[b]		River input (mol/yr)
	mol/yr	% river input	mol/yr	% river input	
SO_4	−1.1E+12	−34	−1.3E+12	−40	3.20E+12[c]
NH_4	7.9E+09	0.3	2.1E+10	0.8	2.55E+12[d]
SiO_2	1.8E+10	0.4	2.2E+11	4	5.00E+12[e]
Ca	4.7E+12	39	4.2E+12	35	1.20E+13[c]
PO_4	−2.6E+08	−0.3	−4.8E+08	−0.6	7.80E+10[f]
Alkalinity	−2.4E+11	−0.7	−1.9E+11	−0.5	3.60E+13[g]

[a] Derived from Baby Bare spring water composition with the assumption that warm ridge-flank hydrothermal sites remove the entire river input of Mg (Sansone et al., 1998; Wheat and Mottl, 2000). The flux of NH_4 was calculated for this study by means of the method and data of Wheat and Mottl (2000).
[b] Basement hydrothermal flux multiplied by the ratio F_{SH}/F_B obtained in simulations of ODP site 1030 (Table 8).
[c] Wheat and Mottl (2000).
[d] Total dissolved N (Jickells, 1995).
[e] Tréguer et al. (1995).
[f] Wheat et al. (1996).
[g] Berner et al. (1983).

drothermal circulation (at all temperatures) may remove as much as 21% of river input of PO_4 (Wheat et al., 1996) and contribute up to 36% of river $SiO_{2(aq)}$ (Kadko et al., 1995), Baby Bare spring water composition suggests that fluxes of PO_4 and $SiO_{2(aq)}$ at warm sites are equivalent to <1% of river input fluxes (Wheat and Mottl, 2000). Fluxes of alkalinity and NH_4 at warm sites are probably also <1% of river input fluxes (Sansone et al., 1998; Wheat and Mottl, 2000). These estimates are based on basement fluid composition. If an insulating sediment blanket is necessary to raise ridge-flank basement temperatures to >45°C, the contribution of reaction with sediment to geochemical fluxes at warm hydrothermal sites is potentially large.

3. MODELING METHODS

We used an updated version of the numerical code Global Implicit Multicomponent Reactive Transport (GIMRT) (Steefel and Yabusaki, 1996; Steefel, 2000) to model the steady-state interaction of sediment and hydrothermal fluid in a one-dimensional domain within which sediment burial, fluid advection, molecular diffusion, organic matter degradation (via O_2 respiration and SO_4 reduction), and inorganic mineral diagenesis occur. Aqueous species included in the model are major seawater solutes and several minor solutes of importance to mineral diagenesis (Table 2). Reactive solid phases included in the model are organic matter, calcite, carbonate fluorapatite (CARFAP), solid iron hydroxide ($Fe(OH)_{3(s)}$), amorphous iron sulfide ($FeS_{(am)}$), and biogenic amorphous silica ($SiO_{2(am)}$). Associated reactions (Table 3) are described in Section 3.2.

3.1. Model Architecture

GIMRT solves the nonlinear set of partial differential equations describing coupled reaction and transport by using finite volume techniques (Steefel and Lasaga, 1994; Steefel and Lichtner, 1994, 1998; Steefel and Yabusaki, 1996; Steefel, 2000). Aqueous, surface complexation, and ion exchange reactions are formulated in this problem as equilibrium reactions. Mineral dissolution and precipitation and oxidation reduction (redox) reactions are formulated as rate-controlled reactions. GIMRT provides several rate law options, including rate laws based on transition state theory for mineral dissolution and precipitation (e.g., Lasaga, 1998) and multiplicative Monod kinetics for organic matter degradation (e.g., Rittmann and Van Briesen, 1996; Van Cappellen and Gaillard, 1996). Although GIMRT has been used previously to simulate reactive transport problems in which molecular diffusion was either dominant (Steefel and Lichtner, 1994) or important (Steefel and Lichtner, 1998; Steefel, 2000), for this study the code has been modified to allow the use of species-specific diffusion coefficients.

3.1.1. Mass Conservation

Mass conservation is maintained on total concentrations of "primary species," a user-specified set of species that provides a complete stoichiometric formula for each species in the system. "Secondary species" are those involved in equilibrium reactions (including sorption) with the primary species. Because concentrations of secondary species can be expressed algebraically in terms of primary species concentrations, separate mass conservation equations are not required (Morel and Hering, 1993; Steefel and MacQuarrie, 1996). The total concentration (T_j) of a primary species is expressed as

$$T_j = C_j + \sum_{i=1}^{N_S} \nu_{ji} C_i, \tag{1}$$

where C_j is the concentration of primary species j (mol/kg water), N_S is the total number of secondary species in the system, ν_{ji} is the stoichiometric coefficient for the secondary species (i.e., the number of moles of primary species j in secondary species i), and C_i is the concentration of secondary species i. The change in T_j with time is given by:

$$\frac{\partial}{\partial t}(\phi \rho T_j) = \frac{\partial}{\partial x}(J_D^{\text{tot}} + J_A^{\text{tot}}) + \sum_{r=1}^{N_r} \nu_{jr} R_r, \tag{2}$$

where ϕ is the porosity and ρ is the fluid density. The first term on the right-hand side accounts for advective (J_A^{tot}) and diffusive (J_D^{tot}) fluxes (x represents depth). The second term on the right-hand side accounts for production and consumption due to kinetically controlled reactions, where N_r is the number of kinetically controlled reactions, R_r is the reaction rate of the rth reaction pathway (units of moles per m^3 porous medium per unit time), and ν_{jr} is the stoichiometric coefficient of primary species j in the rth reaction. Although Eqn. 2 is written in terms of total concentration, GIMRT solves for individual concentrations of primary species and thus effectively folds a speciation calculation into the solution of the governing differential equations (Steefel and Lasaga, 1994).

Conservation equations written in terms of total concentrations of primary species are used in many geochemical (e.g., Morel and Hering, 1993; Parkhurst, 1995) and reactive transport (e.g., Yeh and Tripathi, 1989; Lichtner, 1992, 1996; Steefel and Lasaga, 1994) models, because the formulation allows arbitrary combinations of equilibrium and kinetic reactions provided each species involved in a kinetically controlled reaction is considered a primary species (Steefel and MacQuarrie, 1996). For example, because we consider redox reactions

Table 2. Primary species and boundary condition total concentrations, alkalinity, and pH.

Species	Seawater[a]	Basement water[b] 1030B	Basement water[b] 1031A
	Total concentration (mol/kg)		
$CO_{2(aq)}$	2.37×10^{-3}[e]	3.76×10^{-5}[i]	4.17×10^{-5}[i]
NH_4	3.0×10^{-7}	2.06×10^{-4}	1.00×10^{-4}
Mg	5.2×10^{-2}	5.68×10^{-3}	4.65×10^{-3}
Ca	1.03×10^{-2}	5.712×10^{-2}	6.027×10^{-2}
K	1.01×10^{-2}	6.41×10^{-3}	6.56×10^{-3}
SO_4	2.81×10^{-2}	2.233×10^{-2}	2.342×10^{-2}
H_2PO_4	2.8×10^{-6}	1.3×10^{-8}[j]	2.0×10^{-8}[j]
$SiO_{2(aq)}$	1.9×10^{-4}	2.21×10^{-4}	2.57×10^{-4}
Na[c]	4.662×10^{-1}	4.705×10^{-1}	4.684×10^{-1}
Cl	5.422×10^{-1}	5.577×10^{-1}	5.577×10^{-1}
$H_2S_{(aq)}$	1.0×10^{-15}[f]	1.57×10^{-7}[k]	8.97×10^{-7}[k]
Fe[d]	6.0×10^{-10}[f]	3.3×10^{-6}	7.0×10^{-7}
Mn[d]	5.0×10^{-10}[f]	3.18×10^{-5}	9.0×10^{-6}
$B(OH)_{3(aq)}$	4.1×10^{-4}	4.12×10^{-4}	3.29×10^{-4}
F	3.85×10^{-5}[g]	1.71×10^{-5}	8.4×10^{-6}
$O_{2(aq)}$	1.80×10^{-4}[h]	1.0×10^{-15}[f]	1.0×10^{-15}[f]
NO_3	3.92×10^{-5}	1.0×10^{-6}[l]	1.0×10^{-6}[l]
	Alkalinity (Eq/kg)		
	2.50×10^{-3}[m]	4.6×10^{-4}	3.9×10^{-4}
	pH		
	7.9	8.55[m]	8.46[m]

[a] Measured at Baby Bare (Wheat and Mottl, 2000) unless otherwise noted.
[b] Concentration in deepest pore fluid sample unless otherwise noted.
[c] Constrained by charge balance.
[d] Assumed to be all Fe(II) and Mn(II).
[e] Independent parameter in model, but constrained by measured alkalinity and pH.
[f] Arbitrary, essentially 0 mol/kg.
[g] Concentration in shallowest pore fluid sample from ODP site 1030.
[h] Ingall and Van Cappellen (1990).
[i] In equilibrium with $CaCO_3$.
[j] In equilibrium with CARFAP.
[k] In equilibrium with $FeS_{(am)}$.
[l] Baby Bare spring water (Wheat and Mottl, 2000).
[m] Not an independent condition.

kinetically controlled, each redox state of a particular element (e.g., S(-II) and S(VI)) requires definition of a different primary species (e.g., H_2S and SO_4^{2-}).

3.1.2. Advective Flux

The advective flux of a primary species (J_A^{tot} in Eqn. 2) is the sum of the fluxes of dissolved and sorbed species contributing to T_j. Sorbed species (like minerals) are transported only by burial, which is treated as a standard advection term (Berner, 1980). This portion of J_A^{tot} is given by:

$$J_A^{sorbed} = \omega\phi\rho T_j^{sorbed}, \tag{3}$$

where ω is the burial rate and T_j^{sorbed} is the portion of T_j accounted for by sorbed species (in mol/kg water). The advective flux of a dissolved species includes both fluid flow and burial. This portion of J_A^{tot} is given by:

$$J_A^{diss} = \omega\phi\rho T_j^{diss} + \rho q T_j^{diss}, \tag{4}$$

where T_j^{diss} is the portion of T_j accounted for by dissolved species, and q is specific discharge. Sediment compaction is neglected.

3.1.3. Diffusive Flux

The version of GIMRT used in this work is the first to incorporate species-specific diffusion coefficients, which are necessary to capture the behavior of a system, such as that considered here, in which diffusive transport plays an important role. A rigorous treatment of multicomponent diffusion has been widely described in the sediment diagenesis literature (e.g., Lasaga, 1979, 1998; McDuff and Ellis, 1979; Van Cappellen and Gaillard, 1996), although simpler treatments are more commonly implemented (e.g., Boudreau and Canfield, 1993; Van Cappellen and Wang, 1996). Rigorous treatment requires that diffusive fluxes be written in terms of gradients in chemical potential rather than concentration. Doing so introduces gradients in activity coefficients and an electrochemical migration term that maintains electrical neutrality at the macroscopic scale (Lichtner, 1996; Van Cappellen and Gaillard, 1996). For our simulations, gradients in activity coefficients are negligible, because ionic strength is nearly constant and temperature gradients are small. Neglecting gradients in activity coefficients, the diffusive flux of an individual species in one dimension is given by:

$$J_i = -D_i^{pm}\left[\frac{\partial C_i}{\partial x} - \frac{z_i C_i}{\sum_{k=1}^{N_{tot}} z_k^2 C_k D_k^{pm}}\left\{\sum_{l=1}^{N_{tot}} z_l D_l^{pm}\frac{\partial C_l}{\partial x}\right\}\right] \tag{5}$$

where D_i^{pm} is the porous-medium diffusion coefficient for species i, z_i is the charge of species i, and N_{tot} is the total number of species in the system. The first term on the right-hand side represents the Fickian component of the diffusive flux; the second accounts for electrochemical migration (Van Cappellen and Gaillard, 1996). The total diffusive flux of a primary species (J_D^{tot} in Eqn. 2) is obtained by summing diffusive fluxes for all species contributing to T_j (see Appendix). The electrochemical migration term vanishes if diffusion coefficients for all

Table 3. Heterogeneous reactions and their kinetic constants, seafloor concentrations, and reactive surface areas of solid phases.

Phase	Reaction stoichiometry	log k[a]	E[b] (kJ/mol)	K_{ox} (mol/kg)	Concentration[c]	Area[d] (m^2/m^3 bulk)
		Organic matter				
Organic for $O_{2(aq)}$	$(CH_2O)_{106}(NH_3)_{16}(H_3PO_4) + 1380_{2(aq)} \rightarrow 106CO_{2(aq)} + 122H_2O + 16HNO_3 + H_3PO_4$	−10.51[e]	0	2×10^{-5}	1420[e]	NA
Organic for SO_4, 1030	$(CH_2O)_{106}(NH_3)_{16}(H_3PO_4)_{0.5} + 15H^+ + 53SO_4^{2-} \rightarrow 53H_2S + 16NH_4^+ + 0.5HPO_4^{2-} + 106HCO_3^-$	−12.86[f]	0	1.6×10^{-3}	268[f]	NA
Organic for SO_4, 1031	Same as above	−13.00[f]	0		160[f]	NA
		Minerals				
Calcite	$CaCO_3 + H^+ \Leftrightarrow Ca^{2+} + HCO_3^-$	−6.19[g]	63	NA	0.05[h]	1
CARFAP	$Ca_{10}(PO_4)_{4.975}(CO_3)_{1.5}F_{2.075} \Leftrightarrow 10Ca^{2+} + 4.975PO_4^{3-} + 1.5CO_3^{2-} + 2.075F^-$	−10	47[i]	NA	0	1
$SiO_{2(am)}$	$SiO_{2(am)} \Leftrightarrow SiO_{2(aq)}$	−11.2[j]	63[j]	NA	0.004[k]	0.2[f,l]
$FeS_{(am)}$	$FeS_{(am)} + H^+ \Leftrightarrow Fe^{2+} + HS^-$	−9	0	NA	0	1
$Fe(OH)_{3(s)}$	$Fe(OH)_{3(s)} + 0.5H_2S_{(aq)} \Leftrightarrow Fe^{2+} + H_2O + 2OH^- + 0.5S^0$	−4.99[m]	4.5[m]	NA	0.004[n]	0.294[f,l]

[a] Dissolution rate constants at 25°C. Units of k are s^{-1} for organic phases; mol $m^{-2}s^{-1}$ for all minerals except $Fe(OH)_{3(s)}$; $m^{-2}s^{-1}$ for $Fe(OH)_{3(s)}$ due to first-order dependence on $T_{H_2S_{(aq)}}$.
[b] Activation energy.
[c] Concentration; units are (mol C)/(m^3 bulk volume) for organic phases and (m^3/m^3 bulk volume) for minerals.
[d] Reactive surface area.
[e] Ingall and Van Cappellen (1990).
[f] Determined in this study.
[g] Chou et al. (1989).
[h] Based on values reported by Davis et al. (1997).
[i] Van Cappellen and Berner (1991) (value for fluorapatite).
[j] Van Cappellen and Qiu (1997b).
[k] Based on values reported by Wheat and Tribble (1994).
[l] Equal to 2.4×10^{-5} m^2/g for both $SiO_{2(am)}$ and $Fe(OH)_{3(s)}$.
[m] Yao and Millero (1996).
[n] Based on values reported by Canfield (1989).

aqueous species in the system are the same. The inclusion of this term in the case of unequal diffusion coefficients introduces a slight curvature into what would otherwise be a linear profile for a conservative ion undergoing pure diffusive transport at steady state.

We modeled diffusion of the primary and secondary species that contributed the most to mass balance calculations by using temperature-dependent, species-specific diffusion coefficients, measured in seawater or corrected for the viscosity of seawater (Table 4) (Wollast and Garrels, 1971; Li and Gregory, 1974; Boudreau and Canfield, 1993). For all other species we used a temperature-dependent diffusion coefficient with a value at 25°C of 0.9×10^{-9} m^2/s. Temperature dependence was calculated from the Arrhenius equation (Lasaga, 1998) by using an activation energy of 19 kJ/mol. We calculated diffusion coefficients appropriate for a porous medium according to (McDuff and Ellis, 1979):

$$D_i^{pm} = \frac{D_i^f}{\phi F} \tag{6}$$

where D_i^f is the temperature-corrected diffusion coefficient in the fluid, ϕ is porosity (equal to 0.7), and F is formation factor (equal to 3) (Davis et al., 1997).

3.1.4. Equilibrium Constants

GIMRT employs true thermodynamic equilibrium constants (functions of temperature and pressure only) and calculates species activities by using the extended Debye-Hückel formula with an additional correction for ionic strength (the B-dot formulation) and temperature dependent constants (Helgeson, 1969; Johnson et al., 1992). This

Table 4. Species-specific diffusion coefficients at 25°C.

Cations	D^f (m^2/s)	Anions	D^f (m^2/s)	Neutral species	D^f (m^2/s)
H^+	8.57E − 09[a]	OH^-	4.85E − 09[a]	$CO_{2(aq)}$	1.76E − 09[b]
Na^+	1.22E − 09[a]	Cl^-	1.87E − 09[a]	$H_2S_{(aq)}$	1.79E − 09[b]
K^+	1.80E − 09[a]	F^-	1.34E − 09[a]	$NH_{3(aq)}$	2.07E − 09[b]
Mg^{2+}	6.49E − 10[a]	HCO_3^-	1.09E − 09[a]	$B(OH)_{3(aq)}$	1.11E − 09[b]
Ca^{2+}	7.30E − 10[a]	CO_3^{2-}	8.79E − 10[a]	$B(OH)_4$	9.70E − 10[b]
Fe^{2+}	6.61E − 10[a]	HSO_4^-	1.22E − 09[a]	$SiO_{2(aq)}$	1.00E − 09[c]
NH_4^+	1.82E − 09[a]	SO_4^{2-}	9.84E − 10[a]	$O_{2(aq)}$	2.08E − 09[b]
Mn^{2+}	6.33E − 10[a]	HS^-	1.59E − 09[a]		
		$H_2PO_4^-$	7.78E − 10[a]		
		HPO_4^{2-}	6.75E − 10[a]		
		PO_4^{3-}	5.63E − 10[a]		
		NO_3^-	1.77E − 09[b]		

[a] Li and Gregory (1974), corrected for the viscosity of seawater.
[b] Boudreau and Canfield (1993), corrected for the viscosity of seawater.
[c] Wollast and Garrels (1971), measured in seawater.

Table 5. Thermodynamic stability constants of minerals.[a]

	log K at listed temperature (°C)				
Mineral	0	10	20	30	40
Calcite	2.3931	2.2269	2.064	1.9049	1.7496
CARFAP[b]	−97.9475	−98.3385	−98.7695	−99.2405	−99.7515
$SiO_{2(am)}$[c]	−3.1038	−2.9787	−2.8621	−2.7531	−2.6512
$FeS_{(am)}$[d]	−4.648	−4.648	−4.648	−4.648	−4.648
$Fe(OH)_{3(s)}$	−11.736	−11.6439	−11.6022	−11.6041	−11.6408

[a] For reactions as written in Table 3. Only values for calcite are corrected for pressure. Calculated using SUPCRT (Johnson et al., 1992) unless otherwise noted.
[b] Values at 20°C from Jahnke (1984). Temperature dependence parallels that of fluorapatite.
[c] Van Cappellen and Qiu (1997a).
[d] Value at 25°C. Temperature dependence unavailable.

approach is commonly used to model high-temperature aqueous geochemical systems (e.g., Bowers and Taylor, 1985), but the more common approach for low-temperature seawater systems is to correct for the nonideality of the solution by using seawater-specific activity coefficients or equilibrium constants (e.g., Boudreau and Canfield, 1993). Use of seawater-specific constants produces accurate results for seawater systems and reduces the number of aqueous complexes that need to be included in a model to capture the dependence of mineral solubilities on pH and other variables. The thermodynamic approach used by GIMRT, however, allows systems with pore fluid compositions that differ from seawater (such as those investigated in this article) to be modeled.

We used the code SUPCRT (Johnson et al., 1992) to generate thermodynamic equilibrium constants for the approximate pressure at the seafloor (2600 kPa) and a range of temperatures (0 to 70°C) slightly greater than the observed range (2 to 40°C). The SUPCRT-generated database includes temperature-dependent thermodynamic constants for a large number of aqueous complexation, mineral dissolution, and redox reactions. As described in Section 3.2., we augmented the database with stability constants for solid phases not included in the SUPCRT code (Table 5), and with ion exchange and surface complexation equilibrium constants. Our models included 18 primary aqueous species (Table 2) and 59 secondary aqueous species. Including the large number of secondary species allowed accurate description of mineral solubilities under variable temperature and pH conditions and at ambient pressure conditions.

3.1.5. Rate Laws

We modeled SO_4 reduction and O_2 respiration by using multiplicative Monod kinetics (Rittmann and Van Briesen, 1996; Van Cappellen and Gaillard, 1996; Boudreau, 1997):

$$\text{Rate} = kI \frac{T_{Ox}}{T_{Ox} + K_{ox}} [OM], \tag{7}$$

where k is the rate constant (first order with respect to $[OM]$, the concentration of organic matter), I accounts for inhibition of a reaction pathway by an energetically more favored pathway, T_{Ox} is the total concentration of the electron receptor, and K_{ox} is the half saturation constant (the electron receptor concentration at which the rate becomes half of its maximum value). In simulations that included O_2 respiration, the inhibition of SO_4 reduction was modeled with a hyperbolic function of the form:

$$I = \frac{K_{in}}{K_{in} + T_{O_{2(aq)}}}, \tag{8}$$

where K_{in} is the total concentration of O_2 above which SO_4 reduction is inhibited (1 μmol/kg).

We modeled inorganic mineral precipitation and dissolution reactions by using rate laws based on transition state theory (Lasaga, 1998):

$$\text{Rate} = Ak \left(\prod_{i=1}^{N_E} \alpha_i^p \right) \left(1 - \frac{Q}{K} \right), \tag{9}$$

where A is the surface area of the mineral and k is the temperature-dependent, far-from-equilibrium rate constant for dissolution. The term Πa_i^p gives the far-from-equilibrium dependence on activities of dissolved species: N_E is the total number of species affecting the far-from-equilibrium rate of the reaction, a_i is the activity of species i, and p is the empirically determined exponential dependence. Alternatively, a_i may be replaced with T_j, the total concentration of a primary species. The term $(1 - Q/K)$, where Q is the ion activity product and K is the thermodynamic constant, is the saturation state of the fluid with respect to the mineral. We calculated the temperature dependence of rate constants by using the Arrhenius equation (Lasaga, 1998) and the activation energies listed in Table 3.

3.2. Reaction Network

3.2.1. Organic Matter Degradation

Measured pore-water concentrations of SO_4 and NH_4 from ODP sites 1030 and 1031 (Fig. 2) indicate that organic matter degradation via microbially mediated SO_4 reduction occurs throughout the sampled sections. We modeled this process by using an organic solid phase with the composition $(CH_2O)_{106}(NH_3)_{16}(H_3PO_4)_{0.5}$. This stoichiometry is the Redfield ratio for marine organic matter, modified to account for the nonstoichiometric release of PO_4 during O_2 respiration (Ingall and Van Cappellen, 1990), which probably occurs in the uppermost sediment section. We used measured pore water SO_4 and NH_4 to constrain the concentration of reactive organic matter entering the model domain and the rate constant for SO_4 reduction at each site.

Because we do not have pore-water data from depths <1.45 mbsf at either site, we cannot evaluate the extent to which organic matter degradation occurs via other, energetically more favored pathways. Given the sedimentation rate of 4 to 6 cm/ka, O_2 respiration (in the absence of fluid advection) is predicted to consume 90 to 95% of the reactive organic matter deposited on the seafloor (Tromp et al., 1995). At ODP sites 1030 and 1031 O_2 respiration may consume less organic matter than predicted on the basis of sedimentation rate, because the advection-enhanced upward flux of reduced species may consume a large amount of O_2. We included a generic calculation of O_2 respiration in selected runs to qualitatively assess its impact on solute fluxes. We modeled O_2 respiration by using an organic solid phase with a Redfield composition, $(CH_2O)_{106}(NH_3)_{16}(H_3PO_4)$. This stoichiometry results in a conservative estimate of the ratio of P released to C released, which could be as high as 30:106 during O_2 respiration (Ingall and Van Cappellen, 1990). We used the bottom water O_2 concentration, rate constant, and reactive organic matter concentration set forth by Ingall and Van Cappellen (1990) as appropriate for most of the ocean floor. The effect of bioturbation on organic matter distribution is implicitly accounted for within the rate constant (necessary because bioturbation

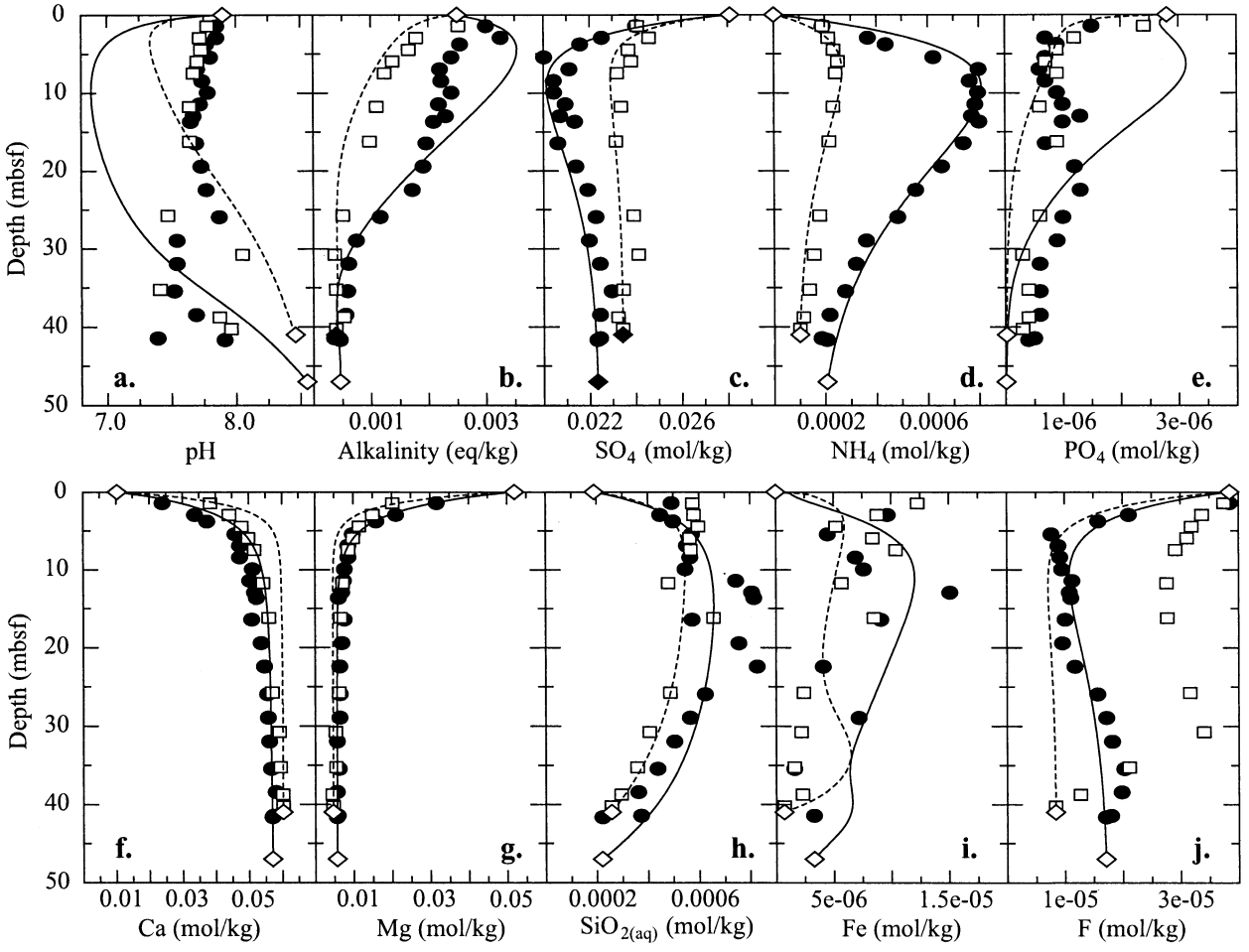

Fig. 2. Pore-water data (Davis et al., 1997; Mottl et al., 2000) and calculated profiles of (a) pH, (b) alkalinity, and total concentrations of (c) SO_4, (d) NH_4, (e) PO_4, (f) Ca, (g) Mg, (h) $SiO_{2(aq)}$, (i) Fe(II), and (j) F for ODP sites 1030 (solid circles and solid lines) and 1031 (open squares and dashed lines). Diamonds = boundary condition concentrations (listed in Table 2).

was not explicitly included in these models) (Ingall and Van Cappellen, 1990).

3.2.2. Calcite

At ODP sites 1030 and 1031 the measured ratio of alkalinity produced to sulfate consumed, which falls below that predicted from organic matter degradation via SO_4 reduction, indicates precipitation of a carbonate mineral. Foraminifera and nannofossils, observed throughout the sediment section at ODP sites 1030 and 1031 (Davis et al., 1997), presumably provide nucleation surfaces for the precipitation of authigenic calcite. In some cases, laboratory-measured rates of calcite dissolution have a high-order dependence on saturation state [$(1 - Q/K)^3$ to $(1 - Q/K)^{11}$] (Morse, 1978; Eisenlohr et al., 1999). We modeled the process by using a linear dependence (Chou et al., 1989), which results in a slower rate far from equilibrium and a faster rate close to equilibrium than obtained with a nonlinear rate law. Either formulation would result in rates of dissolution and precipitation fast enough to keep pore fluids in equilibrium with calcite throughout the model domain.

3.2.3. Carbonate Fluorapatite

At ODP site 1030, the measured F concentrations fall below those predicted by an advective-diffusive model, and the PO_4 concentrations are depressed below those predicted by degradation of organic matter with a C:P ratio of 106:0.5. In other marine sediments, similar modifications to F and PO_4 profiles have been correlated with precipitation of authigenic CARFAP (Froelich et al., 1983; Jahnke et al., 1983; Ruttenberg and Berner, 1993), which can form as a dispersed phase in clay-rich sediments (Ruttenberg and Berner, 1993).

Experimental studies (Jahnke, 1984) and detailed analyses of authigenic CARFAP (Glenn et al., 1988) demonstrated that as the CO_3^{2-} activity of the solution increases, the ratio of CO_3:PO_4 in CARFAP and the solubility of CARFAP both increase. Because the carbonate ion activity of ODP site 1030 and 1031 pore fluids remains similar to or less than that of seawater ($\sim 10^{-6}$ mol/kg) throughout the sediment column, we chose a CO_3:PO_4 ratio (1.5:4.975) and an equilibrium constant at 20°C appropriate for seawater (Jahnke, 1984). We assumed that the temperature dependence of the equilibrium constant for CARFAP was the same as that for fluorapatite, which we calculated by SUPCRT (Johnson et al., 1992) at atmospheric pressure. We chose rate law parameters on the basis of those measured for pure fluorapatite (Van Cappellen and Berner, 1991), but used a linear dependence on saturation state instead of the second order dependence observed for near-equilibrium precipitation of fluorapatite. The linear dependence results in faster rates of CARFAP precipitation than would a second order dependence.

3.2.4. $Fe(OH)_{3(s)}$ and $FeS_{(am)}$

Low sulfide concentrations in ODP site 1030 and 1031 pore waters (less than a few μmol/kg on the basis of the absence of sulfide odor) and the occurrence of pyrite in sediments indicate the presence of poorly crystalline Fe(III)-(hydr)oxide and Fe-sulfide phases. The reductive dissolution of Fe(III)-(hydr)oxides by H_2S, which occurs $\sim 10^7$ times faster than similar reactions involving Fe(III)-silicates, prevents the build up of pore-water sulfide during SO_4 reduction (Canfield, 1989; Canfield et al., 1992) and creates amorphous iron sulfide minerals, precursors to pyrite (Berner, 1970; Rickard, 1974; Yao and Millero, 1996). Concentrations of solid Fe phases other than pyrite were not measured at ODP sites 1030 and 1031. We modeled $Fe(OH)_{3(s)}$ and $FeS_{(am)}$ as the representative phases and chose seafloor concentrations of 0.004 m^3/m^3 for $Fe(OH)_{3(s)}$ ($\sim$120 μmol/cm^3 sediment, similar to concentrations of reactive Fe-oxides measured in Mississippi delta sediments; Canfield, 1989) and 0 m^3/m^3 for $FeS_{(am)}$.

We used a rate law for reductive dissolution of $Fe(OH)_{3(s)}$ that includes a far-from-equilibrium dependence on $T_{H_2S_{(aq)}}$ (Yao and Millero, 1996). Because we used a rate constant for $FeS_{(am)}$ high enough to maintain equilibrium with dissolved Fe^{2+} and $H_2S_{(aq)}$, the rate of reduction of $Fe(OH)_{3(s)}$ controls the rate of formation of $FeS_{(am)}$. This control is consistent with the experimental work of Rickard (1974), which indicated that the rate-controlling step in formation of $FeS_{(am)}$ from sulfidation of goethite is the dissolution of goethite. We did not model the formation of pyrite from $FeS_{(am)}$ and native sulfur (produced by reduction of $Fe(OH)_{3(s)}$), because this reaction does not have a substantial effect on pore-water solute concentrations.

3.2.5. $SiO_{2(am)}$

Measured pore-water silica concentrations, which are too high to be in equilibrium with the abundant quartz, feldspars, or clays (e.g., Mackenzie and Garrels, 1965), indicate that dissolution of $SiO_{2(am)}$ controls the pore-water silica concentration at OPD Sites 1030 and 1031, as it does in most marine sediment (Fanning and Schink, 1969). Although the $SiO_{2(am)}$ content was not measured, radiolarians, diatoms, and sponge spicules were noted in smear slides (Davis et al., 1997). The $SiO_{2(am)}$ concentration in the surface sediments is probably $\sim$1 wt%, similar to that measured in nearby Middle Valley sediments (Wheat and Tribble, 1994) and to that of other sediments underlying low-productivity surface waters (Fanning and Schink, 1969).

We used temperature-dependent solubility constants measured on biogenic silica from a siliceous ooze (Van Cappellen and Qiu, 1997a), a rate law that includes a linear dependence on saturation state, as appropriate for moderately undersaturated fluids (Van Cappellen and Qiu, 1997b), and a rate constant measured in aluminum-rich siliceous ooze (Rabouille et al., 1997; Van Cappellen and Qiu, 1997b).

3.2.6. Ion Exchange and Surface Complexation

In environments where sedimentation rates are high or steady-state pore-water profiles have not developed (e.g., Reimers et al., 1996), adsorption of ions to mineral surfaces can influence pore-water solute concentrations. To test the importance of equilibrium-controlled sorption reactions at ODP sites 1030 and 1031, we ran simulations that included ion exchange (involving Na^+, Mg^{2+}, Ca^{2+}, K^+) or surface complexation (e.g., Dzombak and Morel, 1990; Stumm, 1992) of cations (H^+, Ca^{2+}, Mg^{2+}, Mn^{2+}, Fe^{2+}) and anions (PO_4^{3-}, SO_4^{2-}, CO_3^{2-}, F^-, $H_2BO_3^-$) on $Fe(OH)_{3(s)}$.

We based ion exchange parameters on the cation exchange capacity (15.8 meq/100 g sediment) and equivalent fractions of exchangeable cations [(equivalents adsorbed ion)/(total equivalents adsorbed ions)] measured in surface sediment from ODP site 1030 (Inoue, 2000). We calculated ion exchange equilibrium constants (Table 6) from the measured equivalent fractions of exchangeable cations and the activities of the ions that resulted from speciation of the seawater boundary condition in Table 2 at 25°C. This calculation was made with the assumption that the activity of an absorbed cation is equal to its equivalent fraction (the Gaines-Thomas convention; Appelo and Postma, 1993).

We modeled surface complexation involving "weak" and "strong" sites by means of equilibrium constants for 25°C (Table 7) and a double-layer model to calculate electrostatic corrections as a function of surface charge and pore-water ionic strength (Dzombak and Morel, 1990; Parkhurst, 1995). We used a value of 100 m^2/g for the specific surface area of $Fe(OH)_{3(s)}$ (Yao and Millero, 1996) and site densities of 2.9×10^{-6} and 7.3×10^{-8} moles surface hydroxyls per m^2 mineral for the weak and strong sites, respectively (on the basis of values in Dzombak and Morel, 1990). The amount of each ion complexed to the solid phase at any depth depends on both pore-water composition and the concentration of $Fe(OH)_{3(s)}$.

Table 6. Cation exchange constants.[a]

Exchange reaction[b]	log K
$NaX = Na^+ + X^-$	0
$KX = K^+ + X^-$	−1.31
$CaX_2 = Ca^{2+} + 2X^-$	−2.63
$MgX_2 = Mg^{2+} + 2X^-$	−1.81

[a] Calculated from equivalent fractions measured by Inoue (2000).
[b] X represents a single exchange site.

3.3. Model Domain

The model domain is a one-dimensional sediment column with constant concentration (Dirichlet) boundary conditions at top (bottom seawater) and bottom (basement pore fluid) (Table 2). We imposed a linear thermal gradient from 2°C at the top to 40°C at the bottom in all simulations. We used a node spacing in the top 0.01 m of the sediment column of 1 mm. Below a 0.4-m-long transition zone of gradually increasing node spacing, nodes were spaced 0.5 m apart. Reducing the node spacing at the top of the domain to less than 1 mm altered solute fluxes by less than 1%. Reducing the node spacing throughout the rest of the model domain did not alter results.

Each simulation began with a physically and chemically homogeneous domain. Aqueous phase transport parameters, sediment burial rate, and physical properties of the sediment column were held constant while chemical properties (distribution of reactive solid phases, pore-water chemistry) evolved to steady state values. Instead of modeling sediment accumulation, we modeled a sediment column of constant

Table 7. Surface complexation constants at 25°C.[a]

Complexation reaction	log K
Weak sites	
$>FeO^- + H^+ = >FeOH$	8.93
$>FeOH_2^+ = >FeOH + H^+$	−7.29
$>FeOCa^+ + H^+ = >FeOH + Ca^{2+}$	5.85
$>FeOMg^+ + H^+ = >FeOH + Mg^{2+}$	4.6
$>FeOMn^+ + H^+ = >FeOH + Mn^{2+}$	3.5
$>FeOFe^+ + H^+ = >FeOH + Fe^{2+}$	2.5
$>FeH_2PO_4 + H_2O = >FeOH + PO_4^{3-} + 3H^+$	−31.29
$>FeHPO_4^- + H_2O = >FeOH + PO_4^{3-} + 2H^+$	−25.39
$>FePO_4^{2-} + H_2O = >FeOH + PO_4^{3-} + H^+$	−17.72
$>FeSO_4^- + H_2O = >FeOH + SO_4^{2-} + H^+$	−7.78
$>FeOHSO_4^{2-} = >FeOH + SO_4^{2-}$	−0.79
$>FeH_2BO_3 + H_2O = >FeOH + B(OH)_{3(aq)}$	−0.62
$>FeF + H_2O = >FeOH + F^- + H^+$	−8.7
$>FeOHF^- = >FeOH + F^-$	−1.6
$>FeCO_3^- + H_2O = >FeOH + CO_3^{2-} + H^+$	−12.56
$>FeHCO_3 + H_2O = >FeOH + CO_3^{2-} + 2H^+$	−20.62
Strong sites	
$\gg FeO^- + H^+ = \gg FeOH$	8.93
$\gg FeOH_2^+ = \gg FeOH + H^+$	−7.29
$\gg FeOHCa^{2+} = \gg FeOH + Ca^{2+}$	−4.97
$\gg FeOMn^+ + H^+ = \gg FeOH + Mn^{2+}$	0.4
$\gg FeOFe^+ + H^+ = \gg FeOH + Fe^{2+}$	−0.7

[a] Dzombak and Morel (1990) as implemented by Parkhurst (1995).

thickness through which the solid phase was advected downward. Modeling sediment burial in this way was necessary to obtain the steady-state distribution of reactive solid phases. Because solute transport in the fluid phase occurred at least 20 times faster than sediment burial in all simulations (on the basis of the diffusion length scale), the simulations should provide a good indication of the chemical processes resulting from hydrothermal seepage, despite the inaccurate representation of sediment accumulation.

3.4. Parameter Estimation

To fit calculated profiles to measured pore-water concentrations, it was necessary to estimate (1) specific discharge, (2) concentration of reactive organic material entering the model domain, (3) the rate constant for SO_4 reduction, and (4) the reactive surface areas of $SiO_{2(am)}$ and $Fe(OH)_{3(s)}$. We estimated the first three of these with the nonlinear parameter estimation program PEST (Doherty et al., 1994), which minimizes the least squares error between calculated and measured values by varying the input to and repeatedly calling the forward model (GIMRT). For each site, we first chose a sediment burial rate based on fossil stratigraphy (6 cm/ka and 4 cm/ka, respectively, for ODP sites 1030 and 1031; Davis et al., 1997), then estimated specific discharge by fitting calculated to measured pore-water Mg, which we assume behaves conservatively within the sediment section. We used the resulting specific discharge values for the remainder of the simulations. We next used pore-water SO_4 and NH_4 to estimate the concentration of reactive organic matter entering the model domain and the rate constant for SO_4 reduction. Finally, we adjusted the rate of $SiO_{2(am)}$ dissolution by varying its reactive surface area until calculated $SiO_{2(aq)}$ approximated the data and similarly adjusted the rate of $Fe(OH)_{3(s)}$ dissolution. We did not use the model to constrain any reaction parameters associated with calcite, CARFAP, or $FeS_{(am)}$, because these minerals were essentially in equilibrium with pore fluids in all simulations.

4. MODEL RESULTS

Calculated total concentrations of Mg and of species involved in modeled diagenetic reactions are compared with measured values in Figure 2. Not shown is $T_{H_2S_{(aq)}}$, which remained below $\sim 4 \times 10^{-6}$ mol/kg in all simulations. Calculated pore fluid compositions are in equilibrium with calcite, CARFAP, and $FeS_{(am)}$ throughout the sediment column. They are undersaturated with both $Fe(OH)_{3(s)}$ and $SiO_{2(am)}$. Precipitation and dissolution of minerals resulted in small changes to mineral concentrations. The smallest change was to CARFAP concentration, +0.007 volume % (~0.03 wt% dry) in the simulation of ODP site 1030. The largest change was to calcite concentration, +0.5 volume % (~1.9 wt% dry) in the simulation of ODP site 1030.

The inclusion of O_2 respiration created a 15 cm deep seafloor oxic zone within which calculated pH, alkalinity, and T_{PO_4} were affected. Slightly elevated concentrations of alkalinity and T_{PO_4} persisted to ~10 mbsf in simulations that included O_2 respiration. Because we did not include inorganic N redox reactions or denitrification in the model reaction network, O_2 respiration did not affect T_{NH_4}.

Because of the slow sedimentation rate, the inclusion of multicomponent ion exchange had no effect on calculated steady-state pore-water profiles despite the substantial cation mass incorporated into exchange sites.

The inclusion of surface complexation had a negligible effect on calculated pH. It affected calculated concentrations of solutes and alkalinity on a micromolar scale and thus influenced concentrations of solutes present at the lowest concentrations most significantly. In particular, surface complexation resulted in higher T_{PO_4} (by ~0.5 μm) and lower T_F (by ~2 μm) throughout most of the sediment column, as a result of desorption of PO_4 from sites in equilibrium with seawater within the upper few centimeters of the model domain. Desorption of PO_4 drove precipitation of CARFAP, which lowered the concentration of F. Because we do not have data to constrain processes occurring at depths <1 mbsf, we do not consider surface complexation reactions in the remaining discussion.

Calculated profiles for both sites provide a good match to measured Mg, Ca, SO_4, NH_4, and $SiO_{2(aq)}$ data and thus support the overall modeled reaction network and the use of a steady-state model to approximate the system. Discrepancies between calculated and measured concentrations of alkalinity and PO_4 at ODP site 1030, F at ODP site 1031, and pH and Fe at both sites suggest either that the reaction network used is incomplete or inaccurate in detail, or that the data are affected by sampling artifacts. These discrepancies are discussed further in section 4.2.

4.1. Model-Constrained Parameters

4.1.1. Specific Discharge

Best-fit specific discharge is 1.9 mm/yr at ODP site 1030 and 3.2 mm/yr at ODP site 1031. PEST returns 95% confidence intervals on the basis of the assumption that the relationship between model output (i.e., Mg concentrations) and parameter value (i.e., specific discharge) is linear (Doherty et al., 1994). Subject to this assumption and other assumptions described in Section 3, the upper and lower limits for specific discharge at ODP site 1030 are 2.0 mm/yr and 1.7 mm/yr, respectively. Those for specific discharge at ODP site 1031 are 3.6 mm/yr and 2.8 mm/yr, respectively.

4.1.2. Organic Matter Concentrations and Rate Constants

Best-fit rate constants for SO_4 reduction are $10^{-12.86}$ s^{-1} and $10^{-13.00}$ s^{-1} at ODP sites 1030 and 1031, respectively (Table 3). The constants are consistent with those predicted on the basis of sedimentation rate (Toth and Lerman, 1977). Depth-integrated rates of SO_4 reduction (8.2×10^{-3} and 3.3×10^{-3} mol $SO_4/m^2/yr$ at ODP sites 1030 and 1031, respectively) are consistent with rates calculated for other deep-sea sediments near continental margins (Canfield, 1991).

Model-constrained concentrations of organic carbon entering the top of the model domain represent concentrations entering the SO_4 reduction zone, not seafloor concentrations. Best-fit concentrations are 268 mol C/m^3 bulk and 160 mol C/m^3 bulk at ODP sites 1030 and 1031, respectively, and are similar to total organic carbon concentrations measured in sediments from depths up to 40 mbsf at ODP site 1031 (130 to 290 mol C/m^3 bulk; Davis et al., 1997). They are 16 to 30 times less than the seafloor concentration predicted on the basis of sedimentation rate (Tromp et al., 1995) and 5 to 9 times less than the constant concentration chosen by Ingall and Van Cappellen (1990) as representative of most of the seafloor. These comparisons suggest that 80 to 95% of the reactive organic matter reaching the seafloor at ODP sites 1030 and 1031 is consumed by degradation pathways other than SO_4 reduction.

The rate constant for SO_4 reduction and the organic carbon concentration entering the SO_4 reduction zone are better con-

strained for ODP site 1030 than for ODP site 1031. We used the 95% confidence intervals determined for ODP site 1030 (log $k = -12.95$ to -12.78 and organic carbon concentration = 254 to 283 mol C/m^3 bulk) to assess the influence of small changes in these parameters on seafloor solute fluxes (Section 5).

4.1.3. Reactive Surface Areas

Model-constrained reactive surface areas (2×10^{-5} m^2/g for both $Fe(OH)_{3(s)}$ and $SiO_{2(am)}$) are 10^6 to 10^7 times smaller than physical surface areas assumed or measured in experimental studies (Yao and Millero, 1996; Van Cappellen and Qiu, 1997b). Several possible reasons for these differences exist. (1) The rate constants we used were measured on synthetic $Fe(OH)_{3(s)}$ and on $SiO_{2(am)}$ from surface sediments. The aged, in situ phases may be less reactive because of a combination of adsorption of ions and smoothing of surface defects by recrystallization over time (Yao and Millero, 1996; Rabouille et al., 1997; Van Cappellen and Qiu, 1997b). (2) We used solubility and rate constants measured on $SiO_{2(am)}$ from a siliceous ooze. In the aluminum-rich sediments at ODP sites 1030 and 1031, adsorption of aluminum may decrease both the solubility and the reactivity of $SiO_{2(am)}$, and/or authigenic (amorphous) alumino-silicates may control silica solubility (Rabouille et al., 1997; Van Cappellen and Qiu, 1997a, 1997b; Dixit et al., 2001). (3) The solubility of iron may be affected by the formation of unaccounted for authigenic phases, or the dissolving iron phase might be an Fe(III)-(hydr)oxide that is less reactive than $Fe(OH)_{3(am)}$, such as goethite or hematite (Canfield et al., 1992).

4.2. Model Discrepancies

Discrepancies between measured and calculated pore-water profiles resulted for species whose concentrations are affected by multiple processes both in situ and during sampling. For the upper 20 m of ODP site 1030, calculated alkalinity and T_{PO_4} are higher than measured values (by ~1 mEq/kg and ~1 μmol/kg, respectively), and calculated pH is lower (by ~0.7 log units). For ODP sites 1030 and 1031, calculated $T_{Fe(II)}$ is larger than the measured concentration of Fe.

4.2.1. In Situ Processes

One possible explanation for discrepancies between calculated and measured pH, alkalinity, and PO_4 is that our model of the processes occurring in the sediment column is lacking an in situ reaction capable of buffering pH at higher values. Such a reaction would lower calculated alkalinity and T_{PO_4} through enhanced calcite and CARFAP precipitation. A simulation of ODP site 1030 in which pH was held at 7.6 (approximately equal to the measured pH) throughout the model domain resulted in alkalinity and T_{PO_4} lower than measured (Fig. 3). Increasing the rate of reductive dissolution of $Fe(OH)_{3(s)}$ (e.g., Boudreau and Canfield, 1993) to the point at which siderite ($FeCO_3$) precipitation buffers $T_{Fe(II)}$ at 40 times measured values increased pH only modestly, but did result in calculated alkalinity and T_{PO_4} in the top 20 m of the model domain that more closely match measured values (Fig. 4). We considered

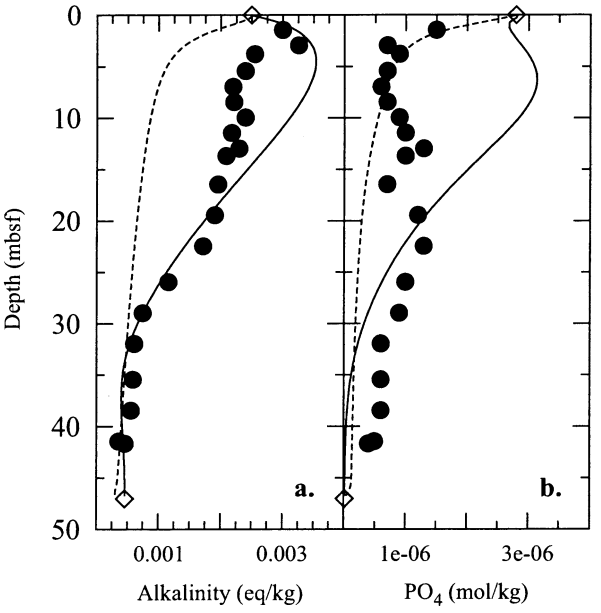

Fig. 3. ODP site 1030 calculated (a) alkalinity and (b) total concentration of PO_4 obtained in a simulation with pH fixed at 7.6 (dashed lines). Other symbols as in Figure 2. Fixed pH simulations were run without multicomponent diffusion.

dissolution and precipitation of several silicate minerals, although our ability to model such reactions was limited by the lack of dissolved Al data. When reactions involving plagioclase, potassium feldspar, illite, saponite, and sepiolite produced reasonable fits to dissolved SiO_2, Ca, K, and Mg data, the reactions had negligible effect on pH.

4.2.2. Potential Sampling Artifacts

Alternatively, changes in pressure and redox environment associated with core retrieval and sampling may have resulted in experimental artifacts.

Alkalinity in pore-water samples collected onboard ship is commonly tens to hundreds of milliequivalents per kilogram less than that of samples collected in situ because of precipi-

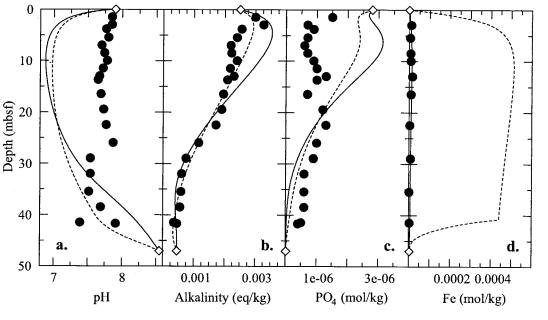

Fig. 4. ODP site 1030 calculated (a) pH, (b) alkalinity, and total concentrations of (c) PO_4 and (d) Fe(II) resulting from fast dissolution of $Fe(OH)_{3(s)}$ and concurrent precipitation of siderite (dashed lines). Other symbols as in Figure 2.

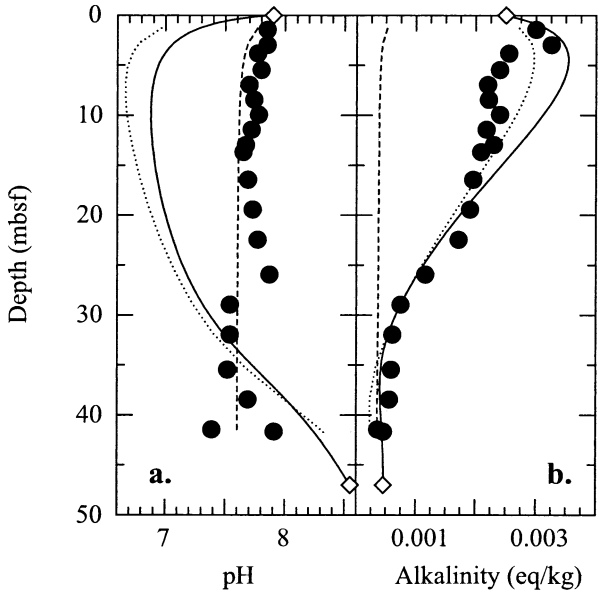

Fig. 5. Equilibration of ODP site 1030 calculated (a) pH and (b) alkalinity at surface temperature and pressure with calcite alone (dotted lines) and with calcite and the partial pressure of atmospheric CO_2 (dashed lines). Other symbols as in Figure 2.

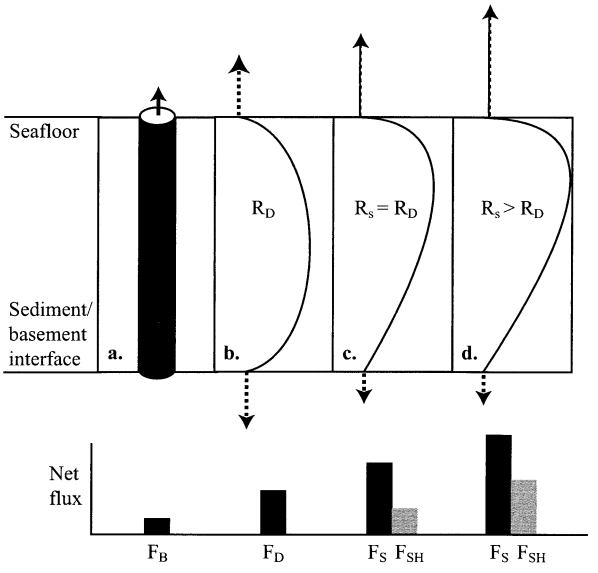

Fig. 6. Flux definitions and illustration of the effect of upward fluid advection on the pore-water profile and sediment hydrothermal flux of a species produced in the sediment column. (a) The basement hydrothermal flux (F_B) results from pipelike discharge of basement fluid into the ocean. (b) The diagenetic flux (F_D) results from diffusion across the seafloor in the absence of flow. Some of the solute produced in the sediment column (at rate R_D) diffuses into basement. (c) The seepage flux (F_S) results from diffusion and advection across the seafloor in the presence of upward fluid advection. The sediment hydrothermal flux (F_{SH}) is the difference between the seepage and diagenetic fluxes. In this illustration, seepage does not change the rate of production of the solute ($R_S = R_D$). F_{SH} exceeds F_B because some of the amount that diffused into basement in (b) now exits at the seafloor. (d) The seepage and sediment hydrothermal fluxes that result when seepage increases the rate of solute production ($R_S > R_D$) are larger than in (c).

tation of calcite during core retrieval (e.g., Murray et al., 1980; Emerson et al., 1982). Calcite precipitation would cause pH to drop (e.g., Murray et al., 1980), but degassing of CO_2 would cause pH to increase during core retrieval. We simulated the equilibration of calculated alkalinity and pH with calcite and atmospheric CO_2 (3.5×10^{-4} atm) at atmospheric pressure and laboratory temperature (18°C) (Fig. 5). Reequilibration of calculated curves with calcite without degassing CO_2 produced alkalinity values very close to measured values. Reequilibration of calculated curves with calcite and complete degassing of CO_2 produced pH very close to measured pH. Some combination of partial equilibration of pore water with calcite and partial degassing of CO_2 may explain the offset between calculated and measured values.

Sampling of anoxic pore waters in the presence of O_2 can cause oxidation of dissolved Fe(II) and precipitation of Fe(III)-(hydr)oxides (Troup et al., 1974; Loder et al., 1978). In experiments documenting this process as much as 50 to 75% of dissolved Fe precipitated (Troup et al., 1974; Loder et al., 1978).

Phosphate deficits of 1 to 3 μmol/kg have been attributed to the decrease in pressure during core retrieval, but the mechanism by which PO_4 is removed from solution is not known (Jahnke et al., 1982, 1989). Because PO_4 adsorbs to both calcite (Avnimelech, 1980) and Fe(III)-(hydr)oxides (Bray et al., 1973), precipitation of either could result in PO_4 removal.

Because sampling artifacts likely affect measured concentrations of several species and no obvious in situ process accounts for differences between calculated and measured profiles, we assume that calculated pore-water concentrations represent in situ values for all species in subsequent flux calculations.

5. SOLUTE FLUXES

5.1. Definitions

To assess how reaction within the sediment column affects solute fluxes, we compared model-derived "sediment hydrothermal fluxes" to "basement hydrothermal fluxes." We defined the sediment hydrothermal flux (F_{SH}) of a species as the difference between the "seepage flux" (F_S, the net seafloor flux resulting from coupled diagenesis and upward seepage of basement fluid) and the "diagenetic flux" (F_D, the diffusive flux across the seafloor resulting from diagenesis in the absence of flow):

$$F_{SH} = F_S - F_D. \tag{10}$$

We defined the basement hydrothermal flux (F_B) of a species as the net advective flux that would result from pipelike flow of basement fluid into the ocean:

$$F_B = q\,(T_{bw} - T_{sw}), \tag{11}$$

where q is specific discharge, T_{bw} is the total concentration of a primary species in basement fluid, and T_{sw} is its total concentration in seawater (Table 2). Flux definitions are schematically illustrated in Figure 6. All fluxes are total fluxes of primary species (analogous to total concentrations). A flux <0

Table 8. Fluxes and depth-integrated reaction rates resulting from various combinations of upward fluid advection and sediment diagenesis.[a]

Species	F_B (mol/m^2/yr)	F_D (mol/m^2/yr)	F_S (mol/m^2/yr)	F_{SH} (mol/m^2/yr)	F_{SH}/F_B	R_D (mol/m^2/yr)	R_S (mol/m^2/yr)
			ODP site 1030				
SO_4	−1.1E-02	−6.4E-03	−1.9E-02	−1.2E-02	1.2	−8.2E-03	−8.2E-03
NH_4	3.7E-04	1.7E-03	2.7E-03	9.9E-04	2.6	2.5E-03	2.5E-03
SiO_2	5.6E-05	2.2E-04	9.1E-04	7.0E-04	12.3	1.3E-03	1.4E-03
Ca	8.5E-02	1.4E-04	7.7E-02	7.6E-02	0.9	−1.1E-02	−8.8E-03
PO_4	−5.1E-06	1.0E-05	8.7E-07	−9.4E-06	1.9	1.0E-05	5.9E-06
Alkalinity	−3.7E-03	5.9E-04	−2.4E-03	−3.0E-03	0.8	−3.6E-03	1.1E-03
			ODP site 1031				
SO_4	−1.5E-02	−3.1E-03	−1.8E-02	−1.5E-02	1.0	−3.3E-03	−3.3E-03
NH_4	3.2E-04	6.9E-04	1.3E-03	5.8E-04	1.8	9.9E-04	9.9E-04
SiO_2	2.1E-04	2.2E-04	1.2E-03	9.6E-04	4.5	1.1E-03	1.3E-03
Ca	1.6E-01	3.2E-03	1.5E-01	1.5E-01	0.9	−6.9E-03	−8.0E-03
PO_4	−8.8E-06	3.7E-06	−1.2E-05	−1.6E-05	1.8	3.7E-06	−3.6E-06
Alkalinity	−6.7E-03	−4.5E-03	−1.5E-02	−1.1E-02	1.6	−6.3E-03	−8.4E-03
			ODP site 1030 with O_2 respiration				
Ca	8.5E-02	3.7E-02	1.1E-01	7.6E-02	0.9	2.2E-02	2.4E-02
PO_4	−4.4E-06	5.2E-04	5.0E-04	−1.7E-05	3.8	5.0E-04	4.9E-04
Alkalinity	−3.7E-03	6.4E-02	6.0E-02	−3.3E-03	0.9	6.6E-02	6.9E-02

[a] A flux >0 indicates a source to the ocean. A rate >0 indicates net production of a solute within the sediment column.

is a flux into the sediment (a sink); a flux >0 is a flux to the ocean (a source).

We quantified the importance of reaction within the sediment column to hydrothermal fluxes of solutes by taking the ratio of sediment hydrothermal flux to basement hydrothermal flux (F_{SH}/F_B). If reaction within the sediment section increases the magnitude of a flux without changing its direction then $F_{SH}/F_B > 1$. If it reverses the direction of a flux (sink becomes a source or vice versa), then $F_{SH}/F_B < 0$.

Coupling upward advection of hydrothermal fluid with sediment diagenesis can create sediment hydrothermal fluxes that differ from basement hydrothermal fluxes in two ways (Fig. 6). First, upward advection increases the size of seafloor concentration gradients and therefore of diffusive fluxes at the seafloor (Fig. 6c). This phenomenon affects fluxes of all species. Second, because upward advection changes the distribution of solutes, rates of mineral precipitation and dissolution that depend on solute concentration change. For aqueous species involved in these reactions, the total (depth-integrated) rate of production in the sediment section in the presence of seepage (R_S) differs from that resulting from diagenesis alone (R_D) (Fig. 6d).

5.2. Dependence on Flow Rate

5.2.1. Slow Flow: Net Fluxes at ODP sites 1030 and 1031

At ODP sites 1030 and 1031 basement fluid is enriched relative to seawater in NH_4, $SiO_{2(aq)}$, and Ca, and depleted in SO_4, PO_4, and alkalinity (Table 2). The basement hydrothermal system is therefore a source of NH_4, $SiO_{2(aq)}$, and Ca and a sink of SO_4, PO_4, and alkalinity. Reaction of upwelling fluid within the sediment section does not reverse the sense of any of these fluxes, but does change the magnitude of all of them (Table 8). Sediment hydrothermal sources of NH_4 and $SiO_{2(aq)}$ are larger than basement hydrothermal sources (F_{SH}/F_B = 2.6 and 12, respectively, at ODP site 1030), and sediment hydrothermal sinks of SO_4 and PO_4 are larger than basement hydrothermal sinks (F_{SH}/F_B = 1.2 and 1.9, respectively, at ODP site 1030). Reaction within the sediment decreases the hydrothermal source of Ca (F_{SH}/F_B = 0.9). It has a variable effect on the hydrothermal sink of alkalinity. At ODP site 1031, the sediment hydrothermal sink of alkalinity is larger than the basement hydrothermal sink (F_{SH}/F_B = 1.6), but at ODP site 1030 it is smaller (F_{SH}/F_B = 0.8).

Variation of the rate constant for SO_4 reduction and of the concentration of organic carbon entering the model domain within the 95% confidence intervals calculated for ODP site 1030 (± ~20% and ± ~5%, respectively) altered flux ratios by a few percent or less (Table 9). Alkalinity was the most sensitive to these parameters with flux ratios altered by ~10%.

Sediment hydrothermal fluxes of SO_4 and NH_4 differ from basement hydrothermal fluxes solely because of the increased seafloor concentration gradients caused by seepage. Seepage does not alter depth-integrated reaction rates of SO_4 and NH_4 ($R_S = R_D$; Table 8), because the rate of organic matter degradation has a negligible dependence on fluid composition (Eqn. 2). Sediment hydrothermal fluxes of $SiO_{2(aq)}$, PO_4, and alkalinity differ from basement hydrothermal fluxes as a result of

Table 9. Sensitivity of F_{SH}/F_B to SO_4 reduction rate.

	Vary k		Vary organic C	
Species	Low[a]	High[b]	Low[c]	High[d]
SO_4	1.1	1.2	1.2	1.1
NH_4	2.5	2.8	2.7	2.5
SiO_2	12.8	12.0	12.3	12.4
Ca	0.9	0.9	0.9	0.9
PO_4	2.0	1.8	1.9	1.9
Alkalinity	0.9	0.7	0.8	0.9

[a] log k = −12.95.
[b] log k = −12.78.
[c] 254 mol C/m^3 bulk.
[d] 283 mol C/m^3 bulk.

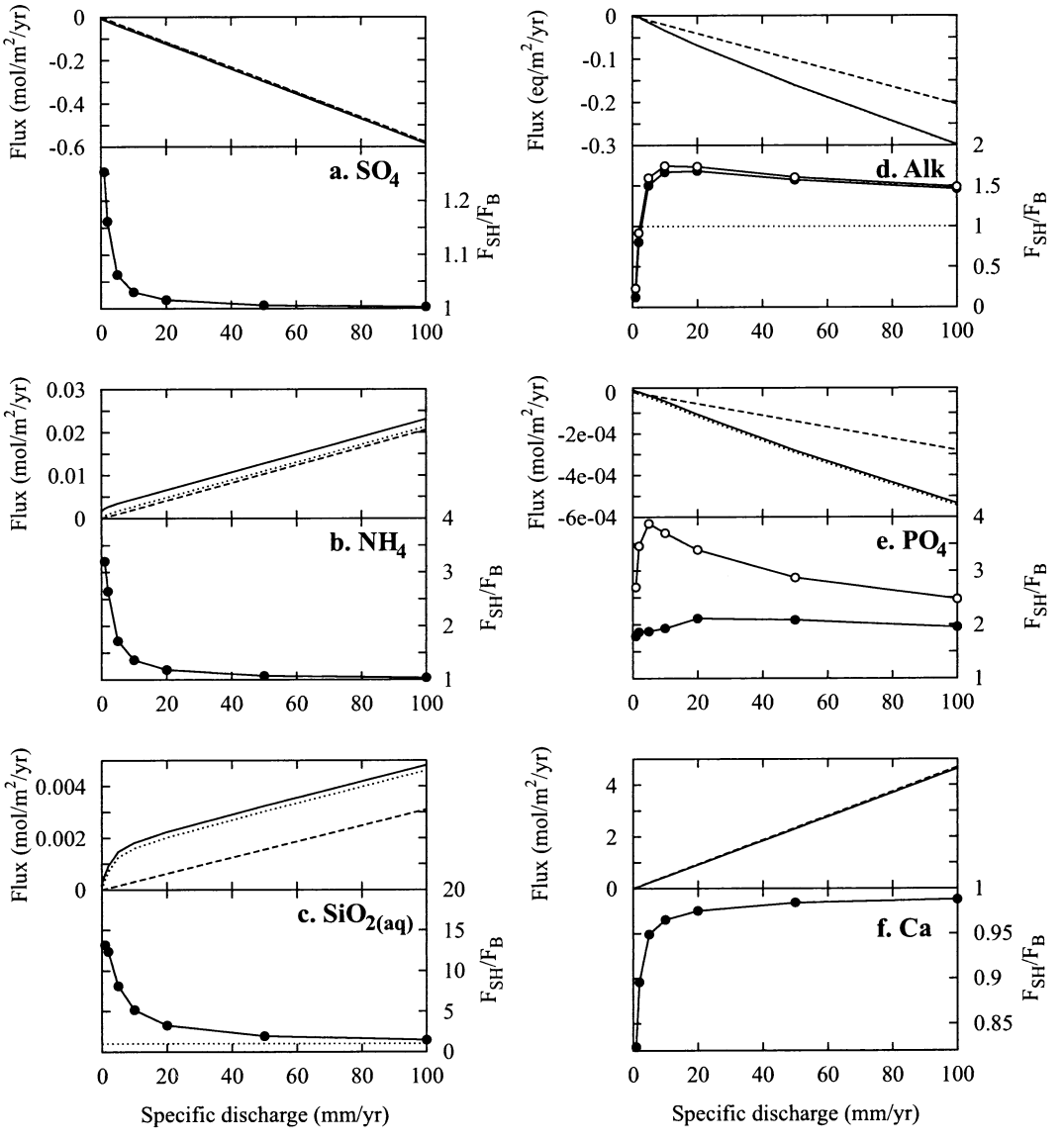

Fig. 7. Net seafloor fluxes resulting from ODP site 1030 parameters as a function of specific discharge. (a) SO_4, (b) NH_4, (c) $SiO_{2(aq)}$, (d) alkalinity, (e) PO_4, (f) Ca. Upper plot of each pair: F_S (solid line), F_B (dashed line), and F_{SH} (dotted line) obtained in simulations that did not include O_2 respiration. ($F_D = F_S$ at 0 mm/yr specific discharge.) Lower plot of each pair: F_{SH}/F_B obtained in simulations that did not include O_2 respiration (solid circles) and in simulations that included O_2 respiration (open circles in plots of PO_4 and alkalinity fluxes). Horizontal dotted line plots at $F_{SH}/F_B = 1$.

differences in depth-integrated reaction rates with and without seepage ($R_S \neq R_D$; Table 8). Seepage increases the rate of $SiO_{2(am)}$ dissolution and of CARFAP precipitation. At ODP site 1031 seepage increases the rate of calcite precipitation, but at ODP site 1030 seepage decreases the rate of calcite precipitation. Despite having opposite effects on calcite precipitation rate at the two sites, upward seepage of fluid has the same effect on hydrothermal fluxes of Ca at both sites, because diagenetic fluxes of Ca are small relative to hydrothermal fluxes (Table 8).

5.2.2. *Faster Flow*

We simulated specific discharge of 1 to 100 mm/yr through a sediment column having all other characteristics identical to ODP site 1030. Rates of upward seepage estimated in ridge flank (crust older than 1 My) settings are typically at the lower end of this range (e.g., Mottl, 1989; Wheat and Mottl, 1994). Faster rates of upward seepage through sediment have been documented on very young crust (<1 My) (e.g., Maris and Bender, 1982; Wheat and McDuff, 1995).

With increasing specific discharge (and increasing basement hydrothermal flux), the relative contribution of reaction within the sediment section to hydrothermal fluxes of SO_4, NH_4, and $SiO_{2(aq)}$ decreased (Fig. 7), because these species have constant rates of production (NH_4 and $SiO_{2(aq)}$) and consumption (SO_4) within the sediment column (R_S is approximately equal to the difference between F_S and F_B in Fig. 7). The contribution of sediment reaction became relatively unimportant to fluxes of

SO_4 and NH_4 at slow to moderate flow rates ($F_{SH}/F_B < 1.1$ at specific discharge >5 mm/yr and $F_{SH}/F_B < 1.1$ at specific discharge >20 mm/yr, respectively). Sediment reaction remained an important hydrothermal source of $SiO_{2(aq)}$ over the range of simulated flow rates ($F_{SH}/F_B = 1.5$ at specific discharge = 100 mm/yr). Extrapolation of the $SiO_{2(aq)}$ fluxes to greater flow rates suggests that the sediment contribution to the hydrothermal flux would remain relatively important ($F_{SH}/F_B > 1.1$) up to flow rates of ~500 mm/yr. The extrapolation may not be valid, however, because the assumption of a linear thermal gradient is not valid for specific discharge >300 mm/yr.

Increasing specific discharge decreased the importance of sediment reaction to hydrothermal fluxes of Ca. At a specific discharge of 100 mm/yr, the sediment hydrothermal flux of Ca differed from the basement hydrothermal flux by <1%.

Increasing specific discharge up to 100 mm/yr had little effect on the relative importance of the sediment column to hydrothermal fluxes of PO_4 ($F_{SH}/F_B \sim 2.0$) and to hydrothermal fluxes of alkalinity at specific discharge ≥5 mm/yr ($F_{SH}/F_B \sim 1.5$). Rate constants for CARFAP and calcite precipitation are high enough to maintain local equilibrium between pore fluids and these minerals. Because the resulting transport-controlled rates of precipitation (R_S) increased with increasing specific discharge, sediment hydrothermal sinks increased more rapidly than basement hydrothermal sinks (Figs. 7d,e). Including O_2 respiration in the simulations resulted in larger sediment hydrothermal sinks of PO_4 and alkalinity at all flow rates.

5.3. Dependence on Sediment Thickness

By use of parameters appropriate for ODP site 1030 and specific discharge of 1.9 and 10 mm/yr, we calculated fluxes through sediment 10 to 100 m thick. Flow rates of 1 to 2 mm/yr have been estimated in areas with as much as 200 m of sediment cover (Mottl, 1989). Flow rates of tens of millimeters per year have only been documented where sediment thickness is less than 50 m (e.g., Maris and Bender, 1982; Wheat and McDuff, 1995).

Over a range of sediment thickness, the sediment hydrothermal flux of a species varies if the size of either the seepage flux or the diagenetic flux varies with sediment thickness (Eqn. 10). Both seepage fluxes and diagenetic fluxes changed with increasing sediment thickness (Fig. 8, upper plots) as a result of increased quantities of reactive solid phases (i.e., organic matter and $SiO_{2(am)}$). Because the boundary condition concentrations and temperatures did not change with sediment thickness, decreasing concentration and temperature gradients drove additional changes in diagenetic fluxes. For instance, the sediment hydrothermal source of Ca increased with increasing sediment thickness (F_{SH}/F_B approached 1) because the diagenetic source of Ca decreased as the distance between the seafloor and the sediment–basement interface increased. For all solutes a faster flow rate (10 mm/yr) decreased the influence of sediment thickness on the relative contribution of the sediment section to hydrothermal fluxes (Fig. 8, lower plots).

For SO_4, NH_4, PO_4, and alkalinity, the response of the sediment hydrothermal flux to sediment thickness was controlled by the length of the SO_4 reduction zone, which reached a maximum of ~47 m in these models. A sediment thickness of 40 to 47 m resulted in maximum ratios of F_{SH}/F_B for SO_4 (1.2) and NH_4 (2.6), a minimum ratio for alkalinity (0.8), and an inflection point in the plot of F_{SH}/F_B for PO_4 (Fig. 8, lower plots). As sediment thickness increased beyond 47 m, seepage fluxes of SO_4 and NH_4 changed little (Figs. 8a,b, upper plots), and diagenetic fluxes responded to the increasing distance (and decreasing concentration gradients) between the SO_4 reduction zone and the base of the sediment column. Because the diagenetic sink of SO_4 and source of NH_4 increased, the sediment hydrothermal sink and source decreased. With increasing sediment thickness, lower temperatures within the SO_4 reduction zone caused the diagenetic sources of PO_4 and alkalinity to increase as a result of reduced rates of CARFAP and calcite precipitation (Figs. 8d,e, upper plots). The larger diagenetic sources resulted in larger sediment hydrothermal sinks of PO_4 and alkalinity ($F_{SH}/F_B = 2.4$ and 1.1, respectively, at a sediment thickness of 100 m).

The depth at which organic matter ran out in these simulations is coincident with the length of the sediment column at ODP site 1030, because we set the bottom boundary condition concentrations of SO_4 and NH_4 equal to the concentrations in the deepest pore fluid sample, taken at a depth 5 m above the base of the sediment column. In general, sediment hydrothermal fluxes of SO_4 and NH_4 will be maximized when the length of the sediment column equals the maximum possible length of the SO_4 reduction zone. A larger concentration of organic matter or a slower rate constant for SO_4 reduction would result in maximum sediment hydrothermal fluxes at greater sediment thickness.

The relative importance of the sediment section to hydrothermal fluxes of $SiO_{2(aq)}$ increased with increasing sediment thickness (at a sediment thickness of 100 m, $F_{SH}/F_B = 30$), due primarily to differences in the distribution of $SiO_{2(aq)}$ with and without flow. Warm temperatures caused faster $SiO_{2(am)}$ dissolution at the base of the sediment column than at the top. Without flow, most of the $SiO_{2(aq)}$ thus produced diffused out of the sediment section across the bottom boundary. With flow it exited across the seafloor. Because $SiO_{2(am)}$ persisted to the base of the sediment column over the simulated range of sediment thickness, a thicker sediment column increased the depth-integrated production rate of $SiO_{2(aq)}$ and amplified the effect of fluid flow.

5.4. Global Implications

If a portion of the hydrothermal fluid escaping basement at warm ridge-flank seepage sites passes through sediment, then global estimates of solute fluxes from warm sites need to account for changes in solute concentrations that occur within the sediment. To demonstrate the maximum effect sediment of the type found at ODP sites 1030 and 1031 could have on global fluxes of solutes from warm ridge-flank sites, we multiplied the global flux estimates derived from Baby Bare spring water (basement fluid) composition (Sansone et al., 1998; Wheat and Mottl, 2000) by the ratios of sediment hydrothermal to basement hydrothermal flux determined in this study. For a sediment thickness of 47 m and a specific discharge of 1.9 mm/yr this calculation results in larger fluxes of SO_4, NH_4, $SiO_{2(aq)}$, and PO_4 and smaller fluxes of Ca and alkalinity (Table

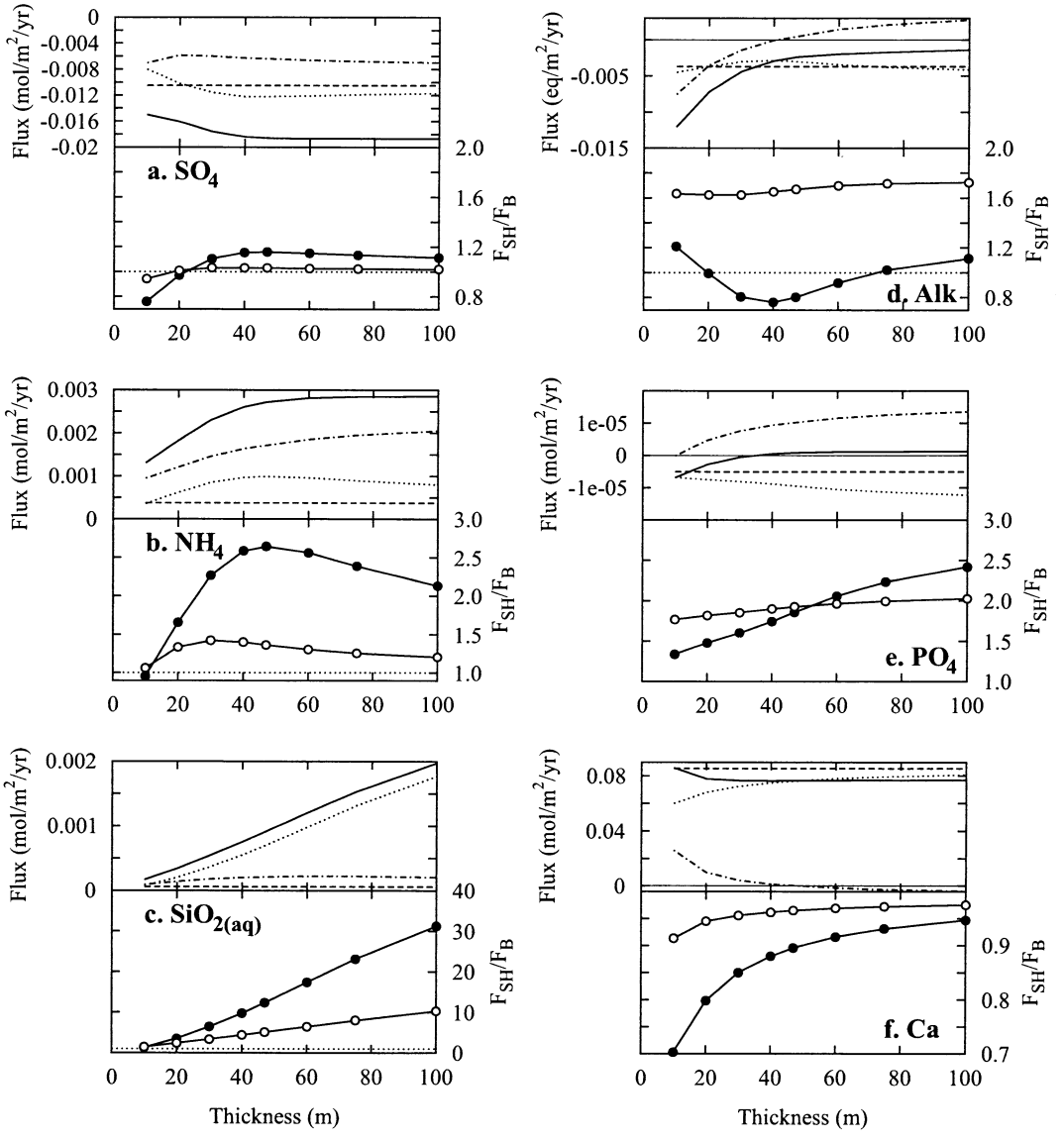

Fig. 8. Net seafloor fluxes resulting from ODP site 1030 parameters as a function of sediment thickness. (a) SO_4, (b) NH_4, (c) $SiO_{2(aq)}$, (d) alkalinity, (e) PO_4, (f) Ca. Upper plot of each pair: F_S (solid line), F_B (dashed line), F_D (dot-dash line), and F_{SH} (dotted line) obtained in simulations with specific discharge = 1.9 mm/yr. Horizontal solid line plots at 0 mol/m^2/yr. Lower plot of each pair: F_{SH}/F_B obtained in simulations with specific discharge = 1.9 mm/yr (solid circles) and in simulations with specific discharge = 10 mm/yr (open circles). Horizontal dotted line plots at $F_{SH}/F_B = 1$.

1). For most species this choice of sediment thickness and specific discharge maximizes the percent difference between the estimate derived from basement fluid composition and the estimate that accounts for reaction within the sediment section. For alkalinity, sediments have a larger and opposite effect at faster flow rates; interaction with sediments (at specific discharge of 5 to 100 mm/yr) could increase the global flux of alkalinity from warm ridge-flank hydrothermal sites to as much as -3.6×10^{11} eq/yr. For PO_4 and $SiO_{2(aq)}$ thicker sediments have a greater effect; interaction with sediments (100 m thick) could increase global fluxes of PO_4 and $SiO_{2(aq)}$ to as much as -7×10^8 mol/yr and 5.4×10^{11} mol/yr, respectively.

Differences between flux estimates that do and do not account for reaction within the sediment section are small in comparison to estimates of river input fluxes for all species except $SiO_{2(aq)}$ (Table 1). Reaction within the sediment section could increase the source of $SiO_{2(aq)}$ from <1% to as much as 11% of river input if interaction of warm hydrothermal fluids with thick (100 m) sediment were ubiquitous. The actual contribution of reaction within the sediment section to warm ridge-flank fluxes will be proportional to the fraction of upwelling hydrothermal fluid that passes through the sediment and must be less than our estimates if this sediment mineralogy and our choice of diagenetic reactions are representative of warm ridge-flank environments. Different sediment mineralogy or reactive organic carbon content would result in different estimates of sediment-influenced hydrothermal fluxes.

6. SUMMARY AND CONCLUSIONS

Estimates of solute fluxes to and from the ocean associated with ridge-flank hydrothermal systems are usually made on the basis of basement pore fluid or mineral composition. We used pore-water geochemical data from ODP sites 1030 and 1031 on the eastern flank of the Juan de Fuca Ridge to examine the influence of reaction within the sediment column on hydrothermal fluxes of solutes at this site of upwelling hydrothermal fluid. We used the reactive-transport code GIMRT to model the processes occurring in the sediment column (including diagenesis, upward fluid flow, sediment burial, and molecular diffusion) and to estimate seafloor fluxes of Ca, $SiO_{2(aq)}$, SO_4, PO_4, NH_4, and alkalinity. Calculated concentrations of solutes best matched measured concentrations with flow rates (specific discharge) of 1.9 mm/yr at ODP site 1030 and 3.2 mm/yr at ODP site 1031 and with the following diagenetic reactions included in the model: organic matter degradation via SO_4 reduction; rate-controlled dissolution of amorphous silica and of amorphous Fe(III)-(hydr)oxide; and (equilibrium) precipitation of calcite, carbonate fluorapatite, and amorphous Fe(II)-sulfide.

At ODP sites 1030 and 1031, basement fluid is enriched relative to seawater in NH_4, SiO_2, and Ca, and depleted in SO_4, PO_4, and alkalinity. The basement hydrothermal system therefore serves as a source of NH_4, SiO_2, and Ca and a sink of SO_4, PO_4, and alkalinity. Reaction of upwelling fluid within the sediment section does not reverse the sense of any of these fluxes, but does change the magnitude of all of them. Reaction within the sediment results in larger hydrothermal sources of NH_4 and $SiO_{2(aq)}$, larger hydrothermal sinks of SO_4 and PO_4, and a smaller hydrothermal source of Ca than would result if basement fluid discharged directly to the ocean without interaction with the sediment section. At ODP site 1031, sediment reaction results in a larger hydrothermal sink of alkalinity, but at ODP site 1030 it results in a smaller sink.

Two series of simulations in which we varied fluid flow rate (1 to 100 mm/yr) and sediment thickness (10 to 100 m) predict that the sediment section will contribute most significantly to fluxes of SO_4 and NH_4 at slow flow rates and intermediate sediment thickness and to fluxes of $SiO_{2(aq)}$ at slow flow rates and large sediment thickness. Reaction within the sediment section could approximately double the hydrothermal sink of PO_4 over a range of flow rates and sediment thickness and could slightly decrease (by $\leq$10%) the size of the hydrothermal source of Ca. Sediment reaction could increase or decrease the hydrothermal sink of alkalinity depending on both flow rate and sediment thickness.

Flux estimates are reliable to the extent that the modeled reaction network provides a reasonable description of the diagenetic processes affecting major ion concentrations within the sediment section. Some of the results reported here suggest that other diagenetic processes may influence hydrothermal fluxes in this and similar settings. Upwelling hydrothermal fluid in the O_2 respiration zone may create hydrothermal sinks of PO_4 and alkalinity in addition to those created in the SO_4 reduction zone. Surface complexation may affect PO_4 fluxes. The aluminum content of the sediment may affect the solubility and reactivity of $SiO_{2(am)}$ (e.g., Dixit et al., 2001) and thus affect $SiO_{2(aq)}$ fluxes.

Our results indicate that upward seepage of warm ridge-flank hydrothermal fluid through the sediment section can significantly increase or decrease local hydrothermal fluxes of solutes. On a global scale the effect of sediment reaction will depend on the fraction of fluid that passes through, rather than bypasses, the sediment. Even if all warm ridge-flank fluid were filtered through the sediment, the resulting increases and decreases in the global hydrothermal fluxes of the solutes considered in this study are likely to be small in comparison to the river input fluxes of these solutes. The sediment section potentially influences the flux of $SiO_{2(aq)}$ the most. Reaction with sediment could increase this flux from $<$1% to several percent of the river input flux.

Acknowledgments—We thank P. Van Cappellen, R. Lowell, B. Boudreau, and an anonymous reviewer for their constructive comments. This work was performed under the auspices of the U.S. Department of Energy by University of California Lawrence Livermore National Laboratory under contract W-7405-Eng-48 and used data provided by the ODP. The ODP is sponsored by the U.S. National Science Foundation and participating countries under management of Joint Oceanographic Institutions Inc.

Associate editor: B. P. Boudreau

REFERENCES

Alt J. C. and Teagle D. A. (1999) The uptake of carbon during alteration of oceanic crust. *Geochim. Cosmochim. Acta* **63,** 1527–1535.

Appelo C. A. J. and Postma D. (1993) *Geochemistry, Groundwater and Pollution.* Balkema.

Avnimelech Y. (1980) Calcium–carbonate–phosphate surface complex in calcareous systems. *Nature* **288,** 255–257.

Bender M. L., Hudson A., Graham D. W., Barnes R. O., Leinen M., and Kahn D. (1985) Diagenesis and convection reflected in pore water chemistry on the western flank of the East Pacific Rise, 20 degrees south. *Earth Planet. Sci. Lett.* **76,** 71–83.

Berner R. A. (1970) Sedimentary pyrite formation. *Am. J. Sci.* **268,** 1–23.

Berner R. A. (1980) *Early Diagenesis: A Theoretical Treatment.* Princeton University Press.

Berner R. A., Lasaga A. C., and Garrels R. M. (1983) The carbonate–silicate geochemical cycle and its effect on atmospheric carbon dioxide over the past 100 million years. *Am. J. Sci.* **283,** 641–683.

Boudreau B. P. (1997) *Diagenetic Models and Their Implementation: Modelling Transport and Reactions in Aquatic Sediments.* Springer-Verlag.

Boudreau B. P. and Canfield D. E. (1993) A comparison of closed- and open-system models for porewater pH and calcite-saturation state. *Geochim. Cosmochim. Acta* **57,** 317–334.

Bowers T. S. and Taylor H. P. (1985) An integrated chemical and stable-isotope model of the origin of midocean ridge hot spring systems. *J. Geophys. Res.* **90,** 12583–12606.

Bray J. T., Bricker O. P., and Troup B. N. (1973) Phosphate in interstitial waters of anoxic sediments: Oxidation effects during sampling procedure. *Science* **180,** 1362–1364.

Canfield D. E. (1989) Reactive iron in marine sediments. *Geochim. Cosmochim. Acta* **53,** 619–632.

Canfield D. E. (1991) Sulfate reduction in deep-sea sediments. *Am. J. Sci.* **291,** 177–188.

Canfield D. E., Raiswell R., and Bottrell S. (1992) The reactivity of sedimentary iron minerals toward sulfide. *Am. J. Sci.* **292,** 659–683.

Chou L., Garrels R. M., and Wollast R. (1989) Comparative study of the kinetics and mechanisms of carbonate minerals. *Chem. Geol.* **78,** 269–282.

Davis E. E., Fisher A. T., Firth J. V., et al. (1997) *Proceedings of the Ocean Drilling Program: Initial Reports,* Vol. 168. Ocean Drilling Program.

Dixit S., Van Cappellen P., and van Bennekom A. J. (2001) Processes

controlling solubility of biogenic silica and pore water build-up of silicic acid in marine sediments. *Mar. Chem.* **73,** 333–352.
Doherty J., Brebber L., and Whyte P. (1994) *PEST.*Watermark Computing.
Dzombak D. A. and Morel F. M. M. (1990) *Surface Complexation Modeling: Hydrous Ferric Oxide.* Wiley.
Eisenlohr L., Meteva K., Gabrovsek F., and Dreybrodt W. (1999) The inhibiting action of intrinsic impurities in natural calcium carbonate minerals to their dissolution kinetics in aqueous H_2O-CO_2 solutions. *Geochim. Cosmochim. Acta* **63,** 989–1002.
Elderfield H., Wheat C. G., Mottl M. J., Monnin C., and Spiro B. (1999) Fluid and geochemical transport through oceanic crust: A transect across the eastern flank of the Juan de Fuca Ridge. *Earth Planet. Sci. Lett.* **172,** 151–165.
Emerson S., Grundmanis V., and Graham D. (1982) Carbonate chemistry in marine porewaters: MANOP sites C and S. *Earth Planet. Sci. Lett.* **61,** 220–232.
Fanning K. A. and Schink D. R. (1969) Interaction of marine sediments with dissolved silica. *Limnol. Oceanogr.* **14,** 59–68.
Fisher A. T., Giambalvo E. R., Sclater J., Kastner M., Ransom B., Weinstein Y., and Lonsdale P. (2001) Heat flow, sediment and pore fluid chemistry, and hydrothermal circulation on the east flank of Alarcon Ridge, Gulf of California. *Earth Planet. Sci. Lett.* **188,** 521–534.
Froelich P. N., Kim K. H., Jahnke R., Burnett W. C., Soutar A., and Deakin M. (1983) Pore water fluoride in Peru continental margin sediments: Uptake from seawater. *Geochim. Cosmochim. Acta* **47,** 1605–1612.
Glenn C. R., Arthur M. A., Yeh H.-W., and Burnett W. C. (1988) Carbon isotopic composition and lattice-bound carbonate of Peru–Chile margin phosphorites. *Mar. Geol.* **80,** 287–307.
Helgeson H. C. (1969) Thermodynamics of hydrothermal systems at elevated temperatures and pressures. *Am. J. Sci.* **267,** 729–804.
Ingall E. D. and Van Cappellen P. (1990) Relation between sedimentation rate and burial of organic phosphorous and organic carbon in marine sediments. *Geochim. Cosmochim. Acta* **54,** 373–386.
Inoue A. (2000) Data report: Exchangeable cation composition of terrigenous hemipelagic sediments in the eastern flank of the Juan de Fuca Ridge. In *Proceedings of the Ocean Drilling Program Scientific Results,* Vol. 168 (eds. A. T. Fisher, E. E. Davis, and C. Escutia), pp. 87–94. Ocean Drilling Program.
Jahnke R. A. (1984) The synthesis and solubility of carbonate fluorapatite. *Am. J. Sci.* **284,** 58–78.
Jahnke R. A., Heggie D., Emerson S., and Grundmanis V. (1982) Pore waters of the central Pacific Ocean: Nutrient results. *Earth Planet. Sci. Lett.* **61,** 233–256.
Jahnke R. A., Emerson S. R., Roe K. K., and Burnett W. C. (1983) The present day formation of apatite in Mexican continental margin sediments. *Geochim. Cosmochim. Acta* **47,** 259–266.
Jahnke R. A., Emerson S. R., Reimers C. E., Schuffert J., Ruttenberg K., and Archer D. (1989) Benthic recycling of biogenic debris in the eastern tropical Atlantic Ocean. *Geochim. Cosmochim. Acta* **53,** 2947–2960.
Jickells T. (1995) Atmospheric inputs of metals and nutrients to the oceans: Their magnitude and effects. *Mar. Chem.* **48,** 199–214.
Johnson J. W., Oelkers E. H., and Helgeson H. C. (1992) SUPCRT92: A software package for calculating the standard molal thermodynamic properties of minerals, gases and aqueous species from 0 to 1000°C and 1 to 5000 bar. *Comp. Geosci.* **18,** 799–847.
Kadko D., Baross J., and Alt J. (1995) The magnitude and global implications of hydrothermal flux. In *Seafloor Hydrothermal Systems: Physical, Chemical, Biological, and Geological Interactions,* Vol. 91, (eds. S. E. Humphris et al.) pp. 446–466. American Geophysical Union.
Kastner M., Gieskes J. M., and Hu J.-Y. (1986) Carbonate recrystallization in basal sediments: Evidence for convective fluid flow on a ridge flank. *Nature* **321,** 158–160.
Lasaga A. C. (1979) The treatment of multi-component diffusion and ion pairs in diagenetic fluxes. *Am. J. Sci.* **279,** 324–346.
Lasaga A. C. (1998) *Kinetic Theory in the Earth Sciences.* Princeton University Press.
Li Y.-H. and Gregory S. (1974) Diffusion of ions in sea water and in deep-sea sediments. *Geochim. Cosmochim. Acta* **38,** 703–714.
Lichtner P. C. (1992) Time-space continuum description of fluid/rock interaction in permeable media. *Water Res. Res.* **28,** 3135–3155.
Lichtner P. C. (1996) Continuum formulation of multicomponent-multiphase reactive transport. In *Reactive Transport in Porous Media,* Vol. 34 (eds. P. C. Lichtner, C. I. Steefel, and E. H. Oelkers), pp. 1–81. Mineralogical Society of America.
Loder T. C., Lyons W. B., Murray S., and McGuinness H. D. (1978) Silicate in anoxic pore waters and oxidation effects during sampling. *Nature* **273,** 373–374.
Mackenzie F. T. and Garrels R. M. (1965) Silicates: Reactivity in sea water. *Science* **150,** 57–58.
Maris C. R. P. and Bender M. L. (1982) Upwelling of hydrothermal solutions through ridge flank sediments shown by pore water profiles. *Science* **216,** 623–626.
McDuff R. E. and Ellis R. A. (1979) Determining diffusion coefficients in marine sediments: A laboratory study of the validity of resistivity techniques. *Am. J. Sci.* **279,** 666–675.
Morel F. and Hering J. (1993) *Principles and Applications of Aquatic Chemistry.* Wiley.
Morse J. W. (1978) Dissolution kinetics of calcium carbonate in sea water: VI. The near-equilibrium dissolution kinetics of calcium carbonate-rich deep sea sediments. *Am. J. Sci.* **278,** 344–353.
Mottl M. J. (1989) Hydrothermal convection, reaction and diffusion in sediments on the Costa Rica Rift flank, pore water evidence from ODP sites 677 and 678. In *Proceedings of the Ocean Drilling Program Scientific Results,* Vol. 111 (eds. K. Becker et al.), pp. 195–214. Ocean Drilling Program.
Mottl M. J. and Wheat C. G. (1994) Hydrothermal circulation through mid-ocean ridge flanks: Fluxes of heat and magnesium. *Geochim. Cosmochim. Acta* **58,** 2225–2237.
Mottl M. J., Wheat G., Baker E., Becker N., Davis E., Feely R., Grehan A., Kadko D., Lilley M., Massoth G., Moyer C., and Sansone F. (1998) Warm springs discovered on 3.5 Ma oceanic crust, eastern flank of the Juan de Fuca Ridge. *Geology* **26,** 51–54.
Mottl M. J., Wheat C. G., Monnin C., and Elderfield H. (2000) Data report. Trace elements and isotopes in pore water from sites 1023 through 1032, eastern flank of the Juan de Fuca Ridge. In *Proceedings of the Ocean Drilling Program Scientific Results,* Vol. 168 (eds. A. T. Fisher, E. E. Davis, and C. Escutia), pp. 105–118. Ocean Drilling Program.
Murray J. W., Emerson S., and Jahnke R. (1980) Carbonate saturation and the effect of pressure on the alkalinity of interstitial waters from the Guatemala Basin. *Geochim. Cosmochim. Acta* **44,** 963–972.
Newman J. S. (1991) *Electrochemical Systems.* Prentice Hall.
Parkhurst D. L. (1995) *User's Guide to PHREEQC: A Computer Program for Speciation, Reaction-Path, Advective-Transport, and Inverse Geochemical Calculations.* U.S. Geological Survey.
Rabouille C., Gaillard J.-F., Tréguer P., and Vincendeau M.-A. (1997) Biogenic silica recycling in surficial sediments across the Polar Front of the Southern Ocean (Indian Sector). *Deep-Sea Res. II* **44,** 1151–1176.
Reimers C. E., Ruttenberg K. C., Canfield D. E., Christiansen M. B., and Martin J. B. (1996) Porewater pH and authigenic phases formed in the uppermost sediments of the Santa Barbara Basin. *Geochim. Cosmochim. Acta* **60,** 4037–4057.
Rickard D. T. (1974) Kinetics and mechanism of the sulfidation of goethite. *Am. J. Sci.* **274,** 941–952.
Rittmann B. E. and Van Briesen J. M. (1996) Microbiological processes in reactive modeling. In *Reactive Transport in Porous Media,* Vol. 34 (eds. P. C. Lichtner, C. I. Steefel, and E. H. Oelkers), pp. 311–334. Mineralogical Society of America.
Ruttenberg K. C. and Berner R. A. (1993) Authigenic apatite formation and burial in sediments from non-upwelling, continental margin environments. *Geochim. Cosmochim. Acta* **57,** 991–1007.
Sansone F. J., Mottl M. J., Olson E. J., Wheat C. G., and Lilley M. D. (1998) CO_2-depleted fluids from mid-ocean ridge-flank hydrothermal springs. *Geochim. Cosmochim. Acta* **62,** 2247–2252.
Steefel C. I. (2000) New directions in hydrogeochemical transport modeling: Incorporating multiple kinetic and equilibrium pathways. In *Computational Methods in Water Resources: Proceedings of the XIII International Conference* (eds. L. R. Bentley et al.), pp. 331–338. A. A. Balkema, Rotterdam.
Steefel C. I. and Lasaga A. C. (1994) A coupled model for transport of

multiple chemical species and kinetic precipitation/dissolution reactions with application to reactive flow in single phase hydrothermal systems. *Am. J. Sci.* **294,** 529–592.
Steefel C. I. and Lichtner P. C. (1994) Diffusion and reaction in rock matrix bordering a hyperalkaline fluid-filled fracture. *Geochim. Cosmochim. Acta* **58,** 3595–3612.
Steefel C. I. and Lichtner P. C. (1998) Multicomponent reactive transport in discrete fractures I: Controls on reaction front geometry. *J. Hydrol.* **209,** 186–199.
Steefel C. I. and MacQuarrie K. T. B. (1996) Approaches to modeling of reactive transport in porous media. In *Reactive Transport in Porous Media,* Vol. 34 (eds. P. C. Lichtner, C. I. Steefel, and E. H. Oelkers), pp. 83–129. Mineralogical Society of America.
Steefel C. I. and Yabusaki S. B. (1996) *OS3D/GIMRT: Software for Multicomponent-Multidimensional Reactive Transport—User Manual and Programmer's Guide.* Pacific Northwest National Laboratory.
Stumm W. (1992) *Chemistry of the Solid–Water Interface: Processes at the Mineral–Water and Particle–Water Interface in Natural Systems.* Wiley.
Toth D. J. and Lerman A. (1977) Organic matter reactivity and sedimentation rates in the ocean. *Am. J. Sci.* **277,** 465–485.
Tréguer P., Nelson D. M., Van Bennekom A. J., DeMaster D. J., Leynaert A., and Quéguiner B. (1995) The silica balance in the world ocean: A reestimate. *Science* **268,** 375–379.
Tromp T. K., Van Cappellen P., and Key R. M. (1995) A global model for the early diagenesis of organic carbon and organic phosphorus in marine sediments. *Geochim. Cosmochim. Acta* **59,** 1259–1284.
Troup B. N., Bricker O. P., and Bray J. T. (1974) Oxidation effect on the analysis of iron in the interstitial water of recent anoxic sediments. *Nature* **249,** 237–239.
Van Cappellen P. and Berner R. A. (1988) A mathematical model for the early diagenesis of phosphorous and fluorine in marine sediments: Apatite precipitation. *Am. J. Sci.* **288,** 289–333.
Van Cappellen P. and Berner R. A. (1991) Fluorapatite crystal growth from modified seawater solutions. *Geochim. Cosmochim. Acta* **55,** 1219–1234.
Van Cappellen P. and Gaillard P. (1996) Biogeochemical dynamics in aquatic sediments. In *Reactive Transport in Porous Media,* Vol. 34 (eds. P. C. Lichtner, C. I. Steefel, and E. H. Oelkers), pp. 335–376. Mineralogical Society of America.
Van Cappellen P. and Wang Y. (1996) Cycling of iron and manganese in surface sediments: A general theory for the coupled transport and reaction of carbon, oxygen, nitrogen, sulfur, iron, and manganese. *Am. J. Sci.* **296,** 197–243.
Van Cappellen P. and Qiu L. (1997a) Biogenic silica dissolution in sediments of the Southern Ocean I: Solubility. *Deep-Sea Res. II* **44,** 1109–1128.
Van Cappellen P. and Qiu L. (1997b) Biogenic silica dissolution in sediments of the Southern Ocean II: Kinetics. *Deep-Sea Res. II* **44,** 1129–1149.
Wang Y. and Van Cappellen P. (1996) A multicomponent reactive transport model of early diagenesis: Application to redox cycling in coastal marine sediments. *Geochim. Cosmochim. Acta* **60,** 299–314.
Wheat C. G. and McDuff R. E. (1994) Hydrothermal flow through the Mariana Mounds: Dissolution of amorphous silica and degradation of organic matter on a mid-ocean ridge flank. *Geochim. Cosmochim. Acta* **58,** 2461–2475.
Wheat C. G. and Mottl M. J. (1994) Hydrothermal circulation, Juan de Fuca Ridge eastern flank: Factors controlling basement water composition. *J. Geophys. Res.* **99,** 3067–3080.
Wheat C. G. and Tribble J. S. (1994) Diagenesis of amorphous silica in Middle Valley, Juan de Fuca Ridge. In: *Proceedings of the Ocean Drilling Program,* Vol. 139 (eds. M. J. Motti, E. E. Davis, A. T. Fisher, and J. F. Slack), pp. 341–349. Ocean Drilling Program.
Wheat C. G. and McDuff R. E. (1995) Mapping the fluid flow of the Mariana Mounds ridge flank hydrothermal system: Pore water chemical tracers. *J. Geophys. Res.* **100,** 8115–8131.
Wheat C. G., Feely R. A., and Mottl M. J. (1996) Phosphate removal by oceanic hydrothermal processes: An update of the phosphorous budget in the oceans. *Geochim. Cosmochim. Acta* **60,** 3593–3608.
Wheat C. G. and Mottl M. J. (2000) Composition of pore and spring waters from Baby Bare: Global implications of geochemical fluxes from a ridge flank hydrothermal system. *Geochim. Cosmochim. Acta* **64,** 629–642.
Williams D. L., Green K., van Andel T. H., Von Herzen R. P., Dymond J. R., and Crane K. (1979) The hydrothermal mounds of the Galapagos Rift: Observations with DSRV *Alvin*and detailed heat flow studies. *J. Geophys. Res.* **84,** 7467–7484.
Wollast R. and Garrels R. M. (1971) Diffusion coefficient of silica in seawater. *Nat. Phys. Sci.* **229,** 94.
Yao W. S. and Millero F. J. (1996) Oxidation of hydrogen sulfide by hydrous Fe(III) oxides in seawater. *Mar. Chem.* **52,** 1–16.
Yeh G. T. and Tripathi V. S. (1989) A critical evaluation of recent developments in hydrogeochemical transport models of reactive multichemical components. *Water Res.* **25,** 93–108.

APPENDIX

Formulation of Multicomponent Diffusion

In multicomponent systems, interactions between species in solution result in rates of diffusion that differ from those predicted by Fick's Law. Where nonideal interactions between species occur, gradients in chemical potential (which depends on the activity of a species), not concentration, drive diffusion. The charge imbalance that arises when charged species diffuse at differing rates drives an additional nonadvective flux known as electrochemical migration (Lasaga, 1979; McDuff and Ellis, 1979; Newman, 1991; Lichtner, 1996; Van Cappellen and Gaillard, 1996). Diffusion driven by gradients in chemical potential and electrochemical migration are included in a general expression for nonadvective flux similar to that derived by Van Cappellen and Gaillard (1996). The flux of an individual species is given by

$$J_i = u_i^0 C_i\,(-\nabla\mu_i + z_i F E), \tag{A1}$$

where u_i^0 is the mobility of species i, C_i its concentration, μ_i its chemical potential, z_i its charge, F is Faraday's constant (coulombs/mole), and E, the electrical field, is equal to the gradient in electrical potential, Φ ($E = -\nabla\Phi$). Because pore waters typically remain electrically neutral (there are no imposed currents), the sum of the charge fluxes is zero:

$$\sum_{i=1}^{N_{\text{tot}}} z_i J_i = 0, \tag{A2}$$

where N_{tot} is the total number of species in the system. Combining Eqns. A1 and A2, results in an expression for the electrical field in terms of chemical potential:

$$E = -\nabla\Phi = \frac{\sum_{l=1}^{N_{\text{tot}}} z_l u_l^0 C_l \nabla\mu_l}{F\sum_{k=1}^{N_{\text{tot}}} z_k^2 u_k^0 C_k}, \tag{A3}$$

which is substituted into Eqn. A1 to obtain an expression for diffusion plus electrochemical migration that is written in terms of chemical potential (Van Cappellen and Gaillard, 1996):

$$J_i = -u_i^0 C_i \nabla\mu_i + u_i^0 z_i C_i \frac{\sum_{l=1}^{N_{\text{tot}}} z_l u_l^0 C_l \nabla\mu_l}{\sum_{k=1}^{N_{\text{tot}}} z_k^2 u_k^0 C_k}. \tag{A4}$$

To obtain an expression for flux in terms of concentrations, the chemical potential is expanded to:

$$\mu_i = \mu_i^0 + RT\ln(\gamma_i C_i), \tag{A5}$$

where R is the ideal gas constant, T is temperature (Kelvin), and γ_i is the activity coefficient for species i. The tracer diffusion coefficient is related to the mobility of the ion through the Nernst-Einstein relation (Lasaga, 1998):

$$D_i^f = u_i^0 RT. \tag{A6}$$

A general expression for the nonadvective flux of a solute i in terms of

concentrations and activity coefficients is obtained by differentiating Eqn. A5 and substituting the result and Eqn. A6 into Eqn. A4:

$$J_i = -\left[D_i^f \nabla C_i + D_i^f C_i \nabla \ln \gamma_i - D_i^f z_i C_i \frac{\sum_{l=1}^{N_{tot}} z_l D_l^f (C_l \nabla \ln \gamma_l + \nabla C_l)}{\sum_{k=1}^{N_{tot}} z_k^2 C_k D_k^f} \right]. \quad \text{(A7)}$$

Gradients in ionic strength and temperature are small in the system we are considering, so we neglect the contribution to the flux from the gradients in the logarithms of the activity coefficients. With this approximation, the flux of an individual species becomes:

$$J_i = -\left[D_i^f \nabla C_i - D_i^f z_i C_i \frac{\sum_{l=1}^{N_{tot}} z_l D_l^f \nabla C_l}{\sum_{k=1}^{N_{tot}} z_k^2 C_k D_k^f} \right]. \quad \text{(A8)}$$

The total nonadvective flux of a primary species ($J_j^{tot} = J_D^{tot}$ in Eqn. 2) is found by summing across the fluxes of the individual species contributing to the total concentration of the primary species (Lichtner, 1996):

$$J_j^{tot} = J_j + \sum_{i=1}^{N_s} \nu_{ji} J_i, \quad \text{(A9)}$$

Substituting Eqn. A8 into Eqn. A9, and replacing the tracer diffusion coefficients with diffusion coefficients appropriate for the porous medium, one obtains:

$$J_j^{tot} = -\left[D_j^{pm} \nabla C_j + \sum_{i=1}^{N_g} \nu_{ji} D_i^{pm} \nabla C_i - T_j^e \frac{\sum_{l=1}^{N_{tot}} z_l D_l^{pm} \nabla C_l}{\sum_{k=1}^{N_{tot}} z_k^2 C_k D_k^{pm}} \right], \quad \text{(10)}$$

where the T^e term is defined as

$$T_j^e = z_j D_j^{pm} C_j + \sum_{i=1}^{N_s} \nu_{ji} z_i D_i^{pm} C_i. \quad \text{(A11)}$$

Eqn. A10 can be further transformed to the equation implemented in GIMRT by noting that reactions (including the ones linking primary and secondary species) must be electrically balanced, leading to a charge conservation equation for each reaction in the system (e.g., Lichtner, 1996). The charge conservation equation can be used to obtain the charge of the ith secondary species in terms of the charges of the primary species (Lichtner, 1996):

$$z_i = \sum_{j=1}^{N_c} \nu_{ji} z_j, \quad \text{(A12)}$$

where N_c is the number of primary species in the system. Substituting this result into Eqn. A10 above, factoring primary species charges where appropriate, and noting that summation terms commute, one obtains:

$$J_j^{tot} = -\left[D_j^{pm} \nabla C_j + \sum_{i=1}^{N_s} \nu_{ji} D_i^{pm} \nabla C_i - T_j^e \frac{\sum_{l=1}^{N_c} z_l \left(D_l^{pm} \nabla C_l + \sum_{i=1}^{N_s} \nu_{li} D_i^{pm} \nabla C_i \right)}{\sum_{k=1}^{N_c} z_k T_k^e} \right]. \quad \text{(A13)}$$

This is the equation implemented in GIMRT and the expression given by Lichtner (1996) (eqn. 284) except that the numerator of the last term on the right-hand side is summed over all of the l primary species. The last term on the right-hand side represents the contribution from electrochemical migration and ensures that electroneutrality in the solution is maintained.

When electrochemical migration is modeled, care must be taken to consider only charge-balanced solutions and charge-balanced reactions. A charge imbalanced solution in an initial or boundary condition would generate an unrealistic flux, as would a reaction that generated a net charge. Surface complexation reactions, if not modeled in conjunction with an explicit calculation of the diffuse layer composition, are such reactions. Charge balance is between the solution and the charged mineral surfaces. Because species in solution are mobile and surface species (except for burial) are not, a charge imbalance develops in solution as surface complexation reactions occur (Parkhurst, 1995; Lichtner, 1996). Modeling a diffuse layer that remains immobile and balances the charge on mineral surfaces would ensure that the mobile aqueous phase remains charge-balanced as surface complexation reactions proceed. Parkhurst (1995) presented such a formulation, but it has not been implemented here because of the high computational cost of the calculation.